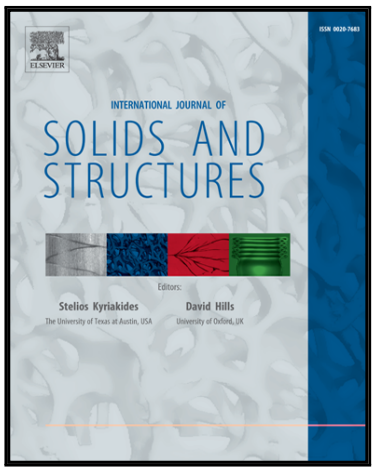

A coupled fluid-solid SPH approach to modelling flow through deformable porous media

Ha H. Bui , Giang D. Nguyen

PII: S0020-7683(17)30286-X
DOI: 10.1016/j.ijsolstr.2017.06.022
Reference: SAS 9629

To appear in: *International Journal of Solids and Structures*

Received date: 20 November 2016
Revised date: 2 May 2017
Accepted date: 18 June 2017

Please cite this article as: Ha H. Bui , Giang D. Nguyen , A coupled fluid-solid SPH approach to modelling flow through deformable porous media, *International Journal of Solids and Structures* (2017), doi: 10.1016/j.ijsolstr.2017.06.022

Highlights

- A new coupled fluid-solid approach to modelling flow through deformable porous media is presented.
- Both solid and fluid phases are evolved in two different Lagrangian discretisations following their own governing equations that are linked through several laws of physics.
- Fully coupled behaviour of fluid and solid is achieved within the two-phase SPH framework by considering the influences of void fractions and solid matrix deformation on the governing equations
- The proposed two-phase SPH model is suitable for modelling long physical time problems owing to the robust and stable explicit ISPH model adopted for the fluid phase.
- The proposed approach is capable of modelling complex problems such as internal erosion due to seepage flow or surface erosion that are challenging to traditional approaches.

A coupled fluid-solid SPH approach to modelling flow through deformable porous media

Ha H. Bui[1] and Giang D. Nguyen[2]

[1]Department of Civil Engineering, Monash University, Australia
[2]School of Civil, Environmental & Mining Engineering, The University of Adelaide, Australia

ABSTRACT

In this paper, a computational framework based on the mesh-free smoothed particle hydrodynamics (SPH) method is developed to study the coupled behaviour of fluid and solid in a deformable porous medium. The mathematical framework developed herein is derived from the Biot's two-phase mixture theory in which the solid is modelled as an elasto-plastic material and the pore-fluid as an incompressible fluid. The key feature of the proposed numerical framework is that both solid and fluid phases are solved simultaneously in two different Lagrangian discretisations (or two different sets of Lagrangian particles) using their own governing equations that are linked through several laws of physics. The capability of the SPH method to model large deformation of the solid materials enables the framework to account for the permeability change due to the dilatant shear behaviour of the solid phase. To obtain a stable and accurate SPH solution for the pore-fluid, an incompressible SPH (ISPH) approach is adapted to correctly simulate the pore-pressure distribution of the fluid phase inside the porous medium. The proposed coupled SPH framework is firstly validated against analytical and solutions obtained using Finite Element Method (FEM) for a submerged soil medium subjected to a gravitational load and a seepage flow through an elastic embankment, respectively. Then, it is employed for the simulation of flows through rockfill dams and an embankment failure induced by seepage flows. Simulation results predicted by SPH show very good agreements with analytical, FEM and experimental results. This suggests that the proposed two-phase SPH framework is a promising approach for future studies of coupled problems that involve complex water free-surface/seepage flows and large deformation of soils which are difficult to be modelled using traditional FEM-based coupled two-phase flow models.

Keywords: SPH, deformable porous media, coupled two-phase flow, large deformation, progressive failure, elasto-plasticity.

1. INTRODUCTION

Coupled flow deformation analysis in saturated and unsaturated porous media is important in many geophysics, engineering applications and industrial processes. Typical examples of these problems include: soil liquefaction during earthquake, gravity driven flows such as fast landslides and debris flows, failure of man-made structure (e.g. dikes and embankments) due to internal seepage erosion or overtopping flows during intensive rainfall and flooding events, oil gas extraction in energy sector or carbon dioxide sequestration in geological formations. All of these applications typically involve complex flow patterns and large deformations of the solid phase that require both an advanced theoretical framework and a robust computational platform to capture the salient mechanisms of the complex multiphase interactions.

The early study of coupled flow-deformation in porous media was mainly based on the concept of single porosity, which is assumed to be fully saturated and consisted of a solid matrix and a single

fluid phase. Any change of stresses in fluid, as a result of dynamic loading, is then accompanied by a corresponding change in the effective stresses in the solid matrix, which produces the deformation of the porous medium. The finite element method (FEM) has been commonly known as a robust numerical tool for solving such single saturated porosity system with many applications ranging from dynamic responses of saturated porous media (Prevost, 1985; Zienkiewicz and Shiomi, 1984), land subsidence above gas/oil reservoirs (Gambolati et al., 2001; Lewis and Sukirman, 1994), multiphase fluid flow in a deforming fractured reservoir (Gelet et al., 2012; Lewis and Ghafouri, 1997), deformation and localisation behaviour of unsaturated soils (Ehlers et al., 2004; Peric et al., 2014), behaviour of soil deposit under seismic loading (Popescu et al., 2006) and landslide triggered by rainfall (Cascini et al., 2010). Although giving satisfactory results, the FEM-based approach has some certain limitations. For instance, it is impossible to simulate complex problems involving flow failure of soils, such as internal erosion due to seepage flow, piping, and/or overtopping flows or transportation of contaminated substances in the subsurface or fractured media, in which the Lagrangian description of fluid flow is explicitly required. Moreover, as FEM is a mesh-based method, it is most suitable for the pre-failure regime with small deformation of the porous media. In the post-failure regime involving large deformations (for example catastrophic landslide with rapid progressive failure and long run distance of soil mass), FEM-based approaches suffer from severe mesh distortion issues even when the updated Lagrangian discretisation or adaptive re-meshing is adopted (Ehlers et al., 2004; Zienkiewicz et al., 1995). In these particular problems, mesh-free methods offer an excellent alternative to model large deformation and failure behaviour saturated/unsaturated porous medium.

In the last few decades, there is a blooming development of mesh-free methods suitable for large deformation analysis such as: smoothed particle hydrodynamics (SPH) (Gingold and Monaghan, 1977; Lucy, 1977), material point method (MPM) (Sulsky, 1996), element free Galerkin method (Belytschko et al., 1994; Krysl and Belytschko, 1996), particle FEM (Onate et al., 2004). Among these methods, SPH is the oldest and truly mesh-free technique whereas other methods are still strongly or weakly based on a computational mesh and therefore have some minor drawbacks such as cell crossing noise in PIC/MPM (Zhang et al., 2011), severe mesh distortions hence re-meshing required in PFEM (Zhang et al., 2013) or high computational cost since both neighbour-searching and mesh-based integration are required in EFG (Duan and Belytschko, 2009). Initially invented for astrophysical applications, the SPH method was quickly developed and successfully applied to various problems in fluid mechanics (Colagrossi and Landrini, 2003; Monaghan, 1994; Shao and Lo, 2003), solid mechanics (Gray et al., 2001; Leroch et al., 2016; Libersky et al., 1993) and geomechanics (Blanc and Pastor, 2013; Bui et al., 2006; Bui et al., 2008; Bui et al., 2011a; Nguyen et al., 2017; Pastor et al., 2009). In the context of coupled flow deformation analysis, Bui et al. (Bui et al., 2007) presented the numerical simulation of soil-water interaction using the SPH method in which both fluid and solid phases were solved simultaneously in two different SPH discretisation platforms using their own set of governing equations. In their approach, the soil matrix was considered as a cohesive-frictional material following an elasto-plastic model, whereas the pore space in the soil skeleton was assumed to be fully saturated with a weakly compressible fluid. The interaction between two constituents (soil skeleton and fluid) was taken into consideration using a seepage force model formulated based on the Darcy's law and the pore-water pressure. Following this framework, numerous studies have been conducted to simulate soil-water interaction problems. For example, Maeda and Sakai (Maeda and Sakai, 2010) studied seepage flow induced failures around sheet piles. In their study, soil was modelled by a non-linear elastic material, while water was treated as a weakly compressible fluid. In these works, the interaction between two phases was calculated using a seepage force model, while ignoring the contribution of the pore-water pressure to the solid phase. Zhang et al. (Zhang and Maeda, 2015) utilised the same approach to study the seepage flow induced dykes and slope failure due to heavy rainfall. Huang et al. (Huang et al., 2013) studied flow process in liquefied soils using the SPH soil-water interaction model in which the soil

was treated as an elastic material. Grabe and Stefanova (Grabe and Stefanova, 2015) investigated hydraulic heave around a retaining wall and seabed erosion around a pipeline. Despite providing some satisfactory results, the above studies based on the two-phase SPH model still have some limitations. For instance, the coupling between soil and fluid in most previous works is weak in the sense that the influence of void fractions on the coupling behaviour of the mixture was not taken into consideration. Despite the fact that the effect of void fractions on soil permeability (and thus on the seepage drag force) was considered in some recent studies such as in (Bui et al., 2011b), the effect of solid matrix deformation on the excess pore-water pressure was totally ignored. In addition, most previous works adopted a weakly compressible SPH approach to simulate the pore-fluid, in which the fluid pressure was calculated using an equation of state formulated as a function of density change. This approach normally suffers from pressure oscillation and thus unable to remain stable for modelling long physical time problems (up to 30 minutes). Finally, the mathematical framework derived in previous works is not fully consistent owing to the simplification of constant void fraction assumption, thus unable to achieve accurate simulation results. The above mentioned shortcomings make those studies, strictly speaking, only suitable for flow through rigid porous media since the pressure fluctuation of the pore-fluid in the weakly compressible SPH model could produce significant error when coupling with the solid phase. Accordingly, it is necessary to further develop the original two-phase SPH model to improve its predictive capability as well as the accuracy of numerical solutions for coupled flow deformation analysis. Within the context of coupled flow deformation analysis, it is also worth to mention the work by Pastor and co-workers (Blanc and Pastor, 2012; Pastor et al., 2009) and Bui and Fukagawa (Bui and Fukagawa, 2009) who followed the *u-p* Biot-Zienkiewicz's approach and used a single set of Lagrangian particles to solve the Biot's mixture theory. Although this approach can simulate complex flow phenomena of rapid landslides and debris flows, the usage of a single set of particles does not provide insights into the mechanism of seepage flows inside the porous structure or the interaction of fluid flows inside and outside the porous medium, and hence might be difficult to model specific occurrences such as internal erosions induced by seepage flows causing empty spaces inside the soil domain, overtopping flow through dams/embankments, surface erosions and water wave impact on geotechnical structures.

In this paper, a two-phase SPH framework is further developed based on the original work by (Bui et al., 2007). The governing equations of the mixture consisting two constituents (fluid and solid skeleton) are fully reformulated taking into consideration the effects of void fractions on the dynamic response of the porous medium as well as the seepage flow. The effect of volumetric deformation of the solid skeleton matrix on the pore-water pressure is taken into consideration for the first time within the SPH context through a consistent mathematical framework that enables stable numerical solutions. In order to obtain a stable numerical solution for the pore-fluid with an accurate pressure profile and to make the two-phase SPH framework suitable for long physical time problems, a fully explicit numerical scheme for incompressible fluid flow (Explicit-ISPH) is adopted. Numerical algorithms for coupling the two-phase system that makes use of the Explicit-ISPH model is also presented. Finally, the proposed two-phase SPH framework is fully validated for both the seepage flow patterns and failure response of the porous medium.

2. MATHEMATICAL FRAMEWORK

In this section, the general mathematical framework describing the coupling procedure of solid and fluid phases is presented to provide the theoretical basis for further development of the two-phase SPH model. The framework is essentially based on the two-phase mixture theory, which was originally developed by (Biot, 1956) for linear elastic materials and further extended to account for nonlinear materials (Prevost, 1980, 1982) and large deformation problems (Zienkiewicz et al., 1999).

2.1. Basic assumptions

The following assumptions are used in the derivation of the generic mathematical framework for coupling the motions of fluid and solid phases in a porous medium:

i. The saturated porous medium is assumed to consist of two constituents (solid skeleton and fluid), each of which moves with their own set of governing equations and occupies the same space at the same time. The interaction between two phases is considered via seepage force, pore-fluid pressure and volumetric deformation (Figure 1).

ii. The Terzaghi's effective stress concept is assumed to be valid and the solid skeleton is modelled using an elasto-plastic model.

iii. Solid grains and fluid flow are assumed to be incompressible. In addition, the fluid phase inside the porous medium is assumed to be Newtonian and the viscosity is negligible.

iv. No mass exchange and heat transfer between two phases are considered in this work.

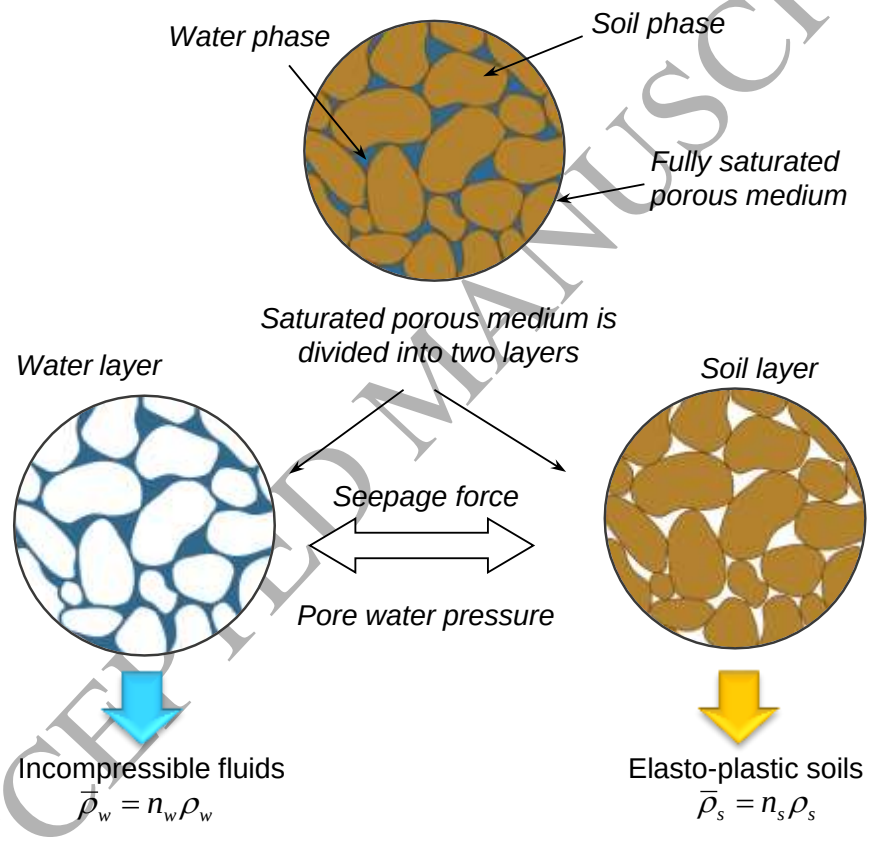

Figure 1: Continuum assumption of saturated porous medium, modified after (Bui et al., 2007)

2.2. Definitions of partial density and partial stress in the porous medium

As discussed, the porous medium considered herein is a two-phase mixture consisting of a soil skeleton and a water phase (Biot, 1956). The pore-space inside the soil skeleton is assumed to be fully saturated with water. Accordingly, the partial densities of the soil and water in the porous medium are respectively defined as:

$$\bar{\rho}_s = n_s \rho_s \tag{1}$$

$$\bar{\rho}_w = n_w \rho_w \tag{2}$$

where ρ_w is the water density; ρ_s is the solid soil density; n_w is the void fraction (or volume fraction) of water; and n_s is the void fraction of soil. The volume fractions of water and soil are related by:

$$n_s + n_w = 1 \tag{3}$$

Using the definitions (1) and (2), the saturated density of mixture is expressed as:

$$\rho_{sat} = \bar{\rho}_f + \bar{\rho}_s = n_w \rho_w + n_s \rho_s \tag{4}$$

Similar to the density, the partial stresses of soil and water are defined respectively as:

$$\bar{\boldsymbol{\sigma}}_s = n_s \boldsymbol{\sigma}_s \tag{5}$$

$$\bar{\boldsymbol{\sigma}}_w = n_w \boldsymbol{\sigma}_w \tag{6}$$

where $\boldsymbol{\sigma}_w$ is the intrinsic stress tensor of water and $\boldsymbol{\sigma}_s$ is the intrinsic stress tensor of soil. The total stress tensor of the saturated mixture $\boldsymbol{\sigma}$ is then the sum of soil and water partial stresses:

$$\boldsymbol{\sigma} = \bar{\boldsymbol{\sigma}}_s + \bar{\boldsymbol{\sigma}}_w = n_s\left(\boldsymbol{\sigma}_s - \boldsymbol{\sigma}_w\right) + \boldsymbol{\sigma}_w \tag{7}$$

The first term in the right hand-side of Equation (7) is often called the "effective stress" in soil mechanics, while the second term is the total stress of water phase consisting of the hydrostatic static pore-water pressure (p_w) and viscous shear stress ($\boldsymbol{\tau}_w$). In soil mechanics, the viscous shear stress of pore-fluid is often ignored, and therefore the stress tensor of the pore-fluid consists of the pore-water pressure only. Using these definitions, the partial stress tensors of soil and water in the porous medium are rewritten as:

$$\bar{\boldsymbol{\sigma}}_s = \boldsymbol{\sigma}' - n_s p_w \mathbf{I} \tag{8}$$

$$\bar{\boldsymbol{\sigma}}_w = -n_w p_w \mathbf{I} \tag{9}$$

where $\mathbf{I}$ is the unit tensor. It should be reminded here that negative stress in the context of this paper means compression.

2.3. Mass balance equations of the deformable porous medium

The mass balance equations for a unit volume of mixture consisting of soil and water phases can be written as follows:

$$\frac{d\bar{\rho}_s}{dt} + \bar{\rho}_s\left(\nabla \cdot \mathbf{v}_s\right) = 0 \tag{10}$$

$$\frac{d\bar{\rho}_w}{dt} + \bar{\rho}_w\left(\nabla \cdot \mathbf{v}_w\right) = 0 \tag{11}$$

where $\mathbf{v}_s$ and $\mathbf{v}_w$ are the velocity vectors of soil and water in the porous medium, respectively. It is noted that Equations (10) and (11) were written under the assumption that the spatial gradient of void fractions over the distribution is sufficiently small, thus can be considered negligible. Substituting Equations (1) and (2) into Equations (10) and (11) yields:

$$\frac{d(n_s \rho_s)}{dt} + n_s \rho_s\left(\nabla \cdot \mathbf{v}_s\right) = 0 \tag{12}$$

$$\frac{d(n_w \rho_w)}{dt} + n_w \rho_w\left(\nabla \cdot \mathbf{v}_w\right) = 0 \tag{13}$$

Equation (12) can be rewritten in the following form:

$$n_s \frac{d\rho_s}{dt} + \rho_s \frac{dn_s}{dt} = -n_s \rho_s \left(\nabla \cdot \mathbf{v}_s\right) \tag{14}$$

Because the deformation of the solid phase (not the solid matrix) is negligible compared to that of the skeleton, the first term on the left hand-side of Equation (14) vanishes, and Equation (14) reduces to:

$$\frac{dn_s}{dt} = -n_s \nabla \cdot \mathbf{v}_s \tag{15}$$

Similarly, Equation (13) can also be rewritten in the following form:

$$n_w \frac{d\rho_w}{dt} + \rho_w \frac{dn_w}{dt} = -n_w \rho_w \left(\nabla \cdot \mathbf{v}_w\right) \tag{16}$$

Substituting Equation (3) into Equation (16) and making use of Equation (15) lead to the following mass balance equation for water phase in the deformable porous medium:

$$\frac{d\rho_w}{dt} = -\rho_w \left(\nabla \cdot \mathbf{v}_w\right) - \rho_w \frac{1-n_w}{n_w} \left(\nabla \cdot \mathbf{v}_s\right) \tag{17}$$

Equation (17) holds for the water flow both inside and outside the porous medium. In the latter case (n_w = 1), the second term in the right hand side of Equation (17) vanishes; thus Equation (17) returns to the standard continuity equation of the fluid flow. In this paper, Equation (15) is solved for the void fraction of solid phase, while the void fraction of water phase is updated using Equation (3). On the other hand, Equation (17) is used to enforce the incompressibility condition of water flow which will be described in Section 2.5.

2.4. Momentum equations of the deformable porous medium

The behaviour of saturated porous medium is determined by the interaction between soil skeleton and pore-fluid, each of which is regarded as a continuum that follows its own governing equations. When the binary phase medium is deformed, the soil skeleton is compressed and pore-fluid flows through the pores. The force acting on the fluid phase due to the soil skeleton, which represents the momentum exchange between two constituents, is defined as (Bowen, 1976):

$$\mathbf{R} = -\frac{\gamma_w n_w^2}{k} \left(\mathbf{v}_w - \mathbf{v}_s\right) + p_w \nabla n_w \tag{18}$$

where **R** is the force per unit volume; γ_w is the specific unit weight of the water; and k is the permeability coefficient. The first term in the right hand-side of Equation (18) is commonly known as the viscous drag force (or seepage force) based on the linear Darcy's law, while the second term is called 'buoyancy term', which is accounted for immiscible mixtures. The coefficient of permeability depends on several factors such as fluid viscosity, pore size distribution, grain size distribution, void ratio and saturation degree of soil. In large deformation analysis, the variation of void ratio results in a significant change of soil permeability that needs to be properly taken into consideration. Various empirical equations for estimating the coefficient of permeability has been reported in the literature (Bear and Cheng, 2010). Among these empirical formulations, the Kozeny-Carman equation is selected in this work to estimate the permeability of soils undergoing large deformation:

$$k = C_k \frac{n_w^3}{\left(1-n_w\right)^2} \tag{19}$$

where C_k is Kozeny-Carman's constant determined from laboratory test.

The momentum equations of the solid and fluid phases in the deformable porous medium are then written as follows:

$$\bar{\rho}_s \frac{d\mathbf{v}_s}{dt} = \nabla \cdot \bar{\boldsymbol{\sigma}}_s + \bar{\rho}_s \mathbf{g} - \mathbf{R} \tag{20}$$

$$\bar{\rho}_w \frac{d\mathbf{v}_w}{dt} = \nabla \cdot \bar{\boldsymbol{\sigma}}_w + \bar{\rho}_w \mathbf{g} + \mathbf{R} \tag{21}$$

By substituting Equations (8) and (9) into Equations (20) and (21) we get:

$$\bar{\rho}_s \frac{d\mathbf{v}_s}{dt} = \nabla \cdot \left(\boldsymbol{\sigma}' - n_s p_w \mathbf{I}\right) + \bar{\rho}_s \mathbf{g} - \mathbf{R} \tag{22}$$

$$\bar{\rho}_w \frac{d\mathbf{v}_w}{dt} = -\nabla(n_w p_w) + \bar{\rho}_w \mathbf{g} + \mathbf{R} \tag{23}$$

Substituting Equation (18) into Equations (22) and (23) and expanding the first terms in the right-hand side of these equations yield:

$$\begin{aligned} \bar{\rho}_s \frac{d\mathbf{v}_s}{dt} &= \nabla \cdot \boldsymbol{\sigma}' - (p_w \nabla n_s + n_s \nabla p_w) + \bar{\rho}_s \mathbf{g} + \frac{\gamma_w n_w^2}{k}(\mathbf{v}_w - \mathbf{v}_s) - p_w \nabla n_w \\ &= \nabla \cdot \boldsymbol{\sigma}' - n_s \nabla p_w + \bar{\rho}_s \mathbf{g} + \frac{\gamma_w n_w^2}{k}(\mathbf{v}_w - \mathbf{v}_s) \end{aligned} \tag{24}$$

$$\begin{aligned} \bar{\rho}_w \frac{d\mathbf{v}_w}{dt} &= -\left(p_w \nabla n_w + n_w \nabla p_w\right) + \bar{\rho}_w \mathbf{g} - \frac{\gamma_w n_w^2}{k}(\mathbf{v}_w - \mathbf{v}_s) + p_w \nabla n_w \\ &= -n_w \nabla p_w + \bar{\rho}_w \mathbf{g} - \frac{\gamma_w n_w^2}{k}(\mathbf{v}_w - \mathbf{v}_s) \end{aligned} \tag{25}$$

Finally, dividing each equation by the corresponding partial density, the following momentum equations for the fluid-solid mixture in the deformable porous medium can be derived:

$$\frac{d\mathbf{v}_s}{dt} = \frac{1}{\bar{\rho}_s}\left(\nabla \cdot \boldsymbol{\sigma}' - n_s \nabla p_w\right) + \mathbf{g} + \frac{\gamma_w n_w^2}{\bar{\rho}_s k}(\mathbf{v}_w - \mathbf{v}_s) \tag{26}$$

$$\frac{d\mathbf{v}_w}{dt} = -\frac{1}{\rho_w}\nabla p_w + \mathbf{g} - \frac{\gamma_w n_w^2}{\bar{\rho}_w k}(\mathbf{v}_w - \mathbf{v}_s) \tag{27}$$

Similar to the continuity Equation (17), Equation (27) holds for inviscid fluid flows both inside and outside the porous medium. For the flow outside the porous medium, such as in the reservoir of an embankment, the seepage force (i.e. the last term) no longer exists, thus Equation (27) returns to the standard momentum equation of inviscid fluids. It is worth to note that, in traditional FEM-based approach, the above momentum equations are further combined to derive a momentum equation for the entire mixture. In this work, a different approach is undertaken by solving the momentum equations of the fluid-solid mixture separately. The advantage of this approach is that the fluid flow through the porous media is explicitly simulated, thus facilitating the modelling of complicated physical problems, such as internal erosion. The proposed SPH framework is, therefore, versatile to simulate and capture several physical phenomena associated with multiphase flows through deformable porous medium.

2.5. Constitutive relations

To complete the above mathematical descriptions of the coupled behaviour of fluid and solid in the

porous medium, a constitutive relation for the mechanical deformation of the porous medium must be specified. Any existing constitutive model capable of describing the elasto-plastic behaviour of the porous medium can be adopted in the current computational framework. For the sake of simplicity, an elasto-plastic constitutive model employing Drucker-Prager yield criterion is chosen. This model was first implemented in the SPH framework by the first author (Bui et al., 2008), and has been shown to be capable of describing large soil deformation with the SPH method (Bui and Fukagawa, 2013; Bui et al., 2011a; Bui et al., 2014; Chen and Qiu, 2012; Deb and Pramanik, 2013; Nguyen et al., 2017). Details of the model derivation can be found in (Bui and Fukagawa, 2013; Bui et al., 2008), and only a brief description of this model is presented here. Following the elasto-plastic framework, the general stress-strain relationship is given as:

$$\dot{\boldsymbol{\sigma}}' = \mathbf{D}^e : \left(\dot{\boldsymbol{\varepsilon}} - \dot{\boldsymbol{\varepsilon}}^p\right) \tag{28}$$

where the dot indicates time derivative, $\mathbf{D}_e$ is the elastic stiffness tensor, $\dot{\boldsymbol{\varepsilon}}$ is the strain rate tensor and $\dot{\boldsymbol{\varepsilon}}^{\mathbf{P}}$ is its plastic component that can be calculated using the plastic flow rule:

$$\dot{\boldsymbol{\varepsilon}}^p = \dot{\lambda}\frac{\partial g_p}{\partial \boldsymbol{\sigma}'} \tag{29}$$

where $\dot{\lambda}$ is the rate of change of plastic multiplier and g_p is the plastic potential function:

$$g_p = \alpha_\psi I_1 + \sqrt{J_2} - \text{constant} \tag{30}$$

In the above expression, I_1 and J_2 are the first and second invariants of the stress tensor, α_ψ is a dilatancy factor that can be related to the dilatancy angle ψ in a fashion similar to that between α_ϕ and friction angle ϕ (see Equation 32). Plastic deformation occurs only if the stress state reaches the yield surface of Drucker-Prager type, defined as:

$$f_y = \alpha_\phi I_1 + \sqrt{J_2} - k_c = 0 \tag{31}$$

where α_ϕ and k_c are Drucker-Prager constants that are calculated from the Coulomb material constants c (cohesion) and ϕ (internal friction). In plane-strain configuration, the Drucker-Prager constants are computed by:

$$\alpha_\phi = \frac{\tan\phi}{\sqrt{9+12\tan^2\phi}} \quad \text{and} \quad k_c = \frac{3c}{\sqrt{9+12\tan^2\phi}} \tag{32}$$

This soil model requires five parameters, which are Young's modulus (E), Poisson's ratio (ν), cohesion coefficient (c), friction angle (ϕ) and dilatancy angle (ψ).

The above elasto-plastic model is established in the effective stress context and therefore neglects the influence of saturation condition of soil. In reality, properties of soil, especially shear strength, are greatly dependent on the saturation condition, or more specifically, on the water content, soil-water characteristic curve and suction. In order to correctly model seepage induced progressive soil failure, the reduction in shear strengths of soil due to the transition behaviour from unsaturated to saturated conditions must be taken into consideration. Advanced unsaturated soil constitutive models (Alonso et al., 1990; Khalili and Loret, 2001; Loret and Khalili, 2000; Sheng et al., 2008) can be used to model the shear strength reduction of soils due to the decrease of soil matrix suction owing to the saturation process. However, implementation of such models in the current SPH framework is beyond the scope of the current paper, and thus is reserved for future works. Alternatively, a simpler approach which based on the general concept in soil mechanics can be applied. It is well known from unsaturated soil mechanics that the change of the degree of saturation of soil does not have a significant effect on the friction angle (Fredlund and Rahardjo, 1993). However, the soil cohesion

strongly depends on the saturation condition. In particular, it is generally accepted that the soil cohesion increases with increasing suction and reduces as the suction decreases. The degradation of suction in soils is, on the other hand, the consequence of the increasing degree of saturation and many empirical relations have been proposed to describe this behaviour (Vangenuchten, 1980). In this work, to account for this behaviour of cohesion, the following linear relationship is adopted:

$$c = c_{sat} + (1 - s_r)(c_o - c_{sat}) \tag{36}$$

where c_o is the initial cohesion at the initial degree of saturation s_r^o; c_{sat} is the apparent cohesion of soil at the fully saturated condition; and s_r is the degree of saturation which ranges from s_r^o to 1.

2.6. Time integration of the governing equations

In the proposed numerical framework, the motions of solid and fluid phases are solved separately using their own governing equations. The solution methods to integrate the governing equations of the solid phase without considering solid-fluid coupling have been explained in details in (Bui et al., 2008), in which the Leap-Frog time integration scheme has been selected to advance solid variables. To avoid repetition, this section will only present relevant solution procedures for the fluid phase. Further details of the coupling procedure are described in Section 3.8.

The two-step prediction and correction time integration scheme method (Shao and Lo, 2003) is selected to solve the governing equations of the incompressible fluid flows, both inside and outside the deformable porous medium. In the first prediction step, intermediate temporal velocity ($\mathbf{v}_w^*$) and position ($\mathbf{r}_w^*$) of the fluid phase is estimated without considering the pressure gradient, using the following equations:

$$\mathbf{v}_w^* = \mathbf{v}_w^t + \left[\mathbf{g} - \frac{\gamma_w n_w^2}{k}(\mathbf{v}_w - \mathbf{v}_s)\right]\Delta t \tag{37}$$

$$\mathbf{r}_w^* = \mathbf{r}_w^t + \mathbf{v}_w^* \Delta t \tag{38}$$

where $\mathbf{v}_w^t$ and $\mathbf{r}_w^t$ are the vector velocity and position at time t, respectively; and Δt is the incremental time. The values of $\mathbf{v}_w^*$ and $\mathbf{r}_w^*$ are then used to compute an intermediate fluid water density as follows:

$$\frac{d\rho_w^*}{dt} = -\rho_w(\nabla \cdot \mathbf{v}_w^*) - \rho_w \frac{1 - n_w}{n_w}(\nabla \cdot \mathbf{v}_s) \tag{39}$$

This equation takes into account the effect of solid matrix deformation through the last term. In the correction step, the force due to the pressure gradient which has been ignored in the first prediction step is taken into consideration to adjust the velocity of fluid phase as follows:

$$\mathbf{v}_w^{t+1} = \mathbf{v}_w^* - \frac{1}{\rho_w^*}\nabla p_w^{t+1}\Delta t \tag{40}$$

where p_w^{t+1} and $\mathbf{v}_w^{t+1}$ are the water pressure and particle velocity at time $(t+1)$.

The pressure at time $(t+1)$ is calculated by enforcing the incompressibility condition for the water fluid phase. This can be done by taking the divergence of Equation (40) and rearranging the obtained equation, leading to:

$$\nabla \cdot \left(\frac{\mathbf{v}_w^{t+1} - \mathbf{v}_w^*}{\Delta t} \right) = \nabla \cdot \left(-\frac{1}{\rho_w^*} \nabla p_w^{t+1} \right) \tag{41}$$

To enforce the incompressibility of the water fluid phase, one needs:

$$\nabla \cdot \left(\frac{\mathbf{v}_w^{t+1}}{\Delta t} \right) = 0 \tag{42}$$

By combining Equations (40) & (41) and making use of the condition (42), the following equation is obtained:

$$\nabla \cdot \left(\frac{1}{\rho^*} \nabla p_w^{t+1} \right) = \frac{1}{\Delta t} \nabla \cdot \mathbf{v}_w^* \tag{43}$$

Alternatively, by substituting Equation (39) into Equation (43), one gets:

$$\nabla \cdot \left(\frac{1}{\rho^*} \nabla p_w^{t+1} \right) = \frac{\rho_w^0 - \rho_w^*}{\rho_w^0 \Delta t^2} - \frac{1 - n_w}{n_w \Delta t} \nabla \cdot \mathbf{v}_s \tag{44}$$

where ρ_w^0 is the initial density of fluid phase. Equations (43) and (44) are equivalent and commonly known as the pressure Poisson's equations for the fluid phase, which can be applied to both flows inside and outside the porous medium. For the latter case, the last term of Equation (44) vanishes, and Equation (44) reduces to the same pressure Poisson's equation derived by (Shao and Lo, 2003) for an incompressible fluid flow. On the other hand, for flows inside a porous medium, the source term on the right hand side of the Poisson's equation consists of both the variations of the fluid phase density and solid void fraction, thus coupling the effect of solid matrix deformation on the pore-water pressure. Details on solving these equations will be further discussed in the next section.

The pressure calculated from either Equation (43) or Equations (44) is then used in Equation (40) to calculate the velocity at time $(t+1)$, and the position at the corresponding time is finally calculated at:

$$\mathbf{r}_w^{t+1} = \mathbf{r}_w^t + \frac{\mathbf{v}_w^t + \mathbf{v}_w^{t+1}}{2} \Delta t \tag{45}$$

where $\mathbf{r}_w^t$ and $\mathbf{r}_w^{t+1}$ are the positions of the particle at time *t* and $(t+1)$, respectively.

The current two-step prediction-correction explicit time integration scheme requires a sufficiently small time step (Δt) to guarantee the stability of the solution. In particular, the time step must satisfy the Courant-Friedrich-Levy (CFL) stability condition:

$$\Delta t \le CFL \min(\Delta t_w, \Delta t_s) \quad with \quad \Delta t_w = l / v_{\max} \ \& \ \Delta t_s = l / c_s \tag{46}$$

where l is the length scale of the numerical discretization; v_{max} is the maximum flow velocity in the computation; c_s is the sound speed of soil; and *CFL* is the Courant number taken to be 0.2.

3. SOLUTION APPROXIMATION USING THE SPH METHOD

3.1. Smoothed particle hydrodynamics (SPH)

In the SPH method, the computational domain is discretised into a finite number of particles. These particles carry material properties (such as velocity, density, stress, etc.) and move with the material velocity according to their governing equations. The material properties of each particle are then

calculated through the use of an interpolation process over its neighbouring particles. The interpolation process is based on the integral representation of a field function:

$$A(\mathbf{r}) = \int_{\Omega} A(\mathbf{r}')W(\mathbf{r}-\mathbf{r}',h)d\mathbf{r}' + O(h^2) \tag{47}$$

where A is any variable defined on the spatial coordinate $\mathbf{r}$ and kernel function W, which is taken to be a cubic-spline function (Monaghan and Lattanzio, 1985), and h is the smoothing function. The integral representation in Equation (47) is then further discretised onto a finite set of interpolation points (the particles), which carry constant mass and other field variables at their corresponding locations, by replacing the integral with a summation and the mass element ρV with the particle mass m:

$$A(\mathrm{r}) = \int_{\Omega} \frac{A(\mathrm{r}')}{\rho(\mathrm{r}')}W(\mathrm{r}-\mathrm{r}',h)\rho(\mathrm{r}')d\mathrm{r}' + O(h^2) \approx \sum_{J=1}^{N} m_J \frac{A_J}{\rho_J} W(\mathrm{r}-\mathrm{r}_J,h) \tag{48}$$

where the subscript J refers to the quantity evaluated at the position of particle J; ρ_J is the density of particle J; m_J is the mass of particle J; and N is the number of "neighbouring particles", i.e., those in the support domain Ω.

The SPH approximation for a gradient term may be calculated by taking the analytical derivative of Equation (48), giving:

$$\nabla A(\mathbf{r}) = \frac{\partial}{\partial \mathbf{r}} \int_{\Omega} \frac{A(\mathbf{r}')}{\rho(\mathbf{r}')}W(\mathbf{r}-\mathbf{r}',h)\rho(\mathbf{r}')d\mathbf{r}' + O(h^2) \approx \sum_{J=1}^{N} m_J \frac{A_J}{\rho_J} \nabla W(\mathbf{r}-\mathbf{r}_J,h) \tag{49}$$

Equations (48) and (49) are the basic SPH formulations, which form all other SPH formalisms in the literature. Further details of the gradient approximations and other issues of the SPH method can be found in (Monaghan, 2012).

3.2. SPH approximations of void fractions

To simplify our discretisation, it is convenient to reserve subscripts i and j for the solid phase, and subscripts a and b for the fluid phase. The variation of the void fraction of the solid phase is calculated by solving Equation (15). By expanding the right hand-side of this equation and applying the SPH approximation (49) to the divergence term, the following SPH approximation for the void fraction of the solid phase can be obtained:

$$\begin{aligned} \frac{dn_i}{dt} &= -\left\{\nabla\cdot(n\mathbf{v}) - \mathbf{v}\cdot(\nabla n)\right\}_i \\ &= -\sum_{j=1}^{N} \frac{\overline{m}_j}{\overline{\rho}_j}(n_j\mathbf{v}_j)\cdot\nabla_i W_{ij} + \sum_{j=1}^{N} \frac{\overline{m}_j}{\overline{\rho}_j}(n_j\mathbf{v}_i)\cdot\nabla_i W_{ij} \\ &= \sum_{j=1}^{N} \frac{\overline{m}_j}{\overline{\rho}_j} n_j(\mathbf{v}_i - \mathbf{v}_j)\cdot\nabla_i W_{ij} \end{aligned} \tag{50}$$

where $\overline{m}_j$ is the mass of particle j, calculated as the product of the partial density (not the solid density) and the spatially discretised volume; and N is the total number of neighbouring particles of particle i. The calculated void fraction of the solid phase is then used to estimate the void fraction of the fluid phase using Equation (3) as follows:

$$n_a = 1 - n_i \tag{51}$$

Because the void fraction of the fluid phase is calculated at the location of a fluid particle rather than

at that of the solid particle, the SPH approximation of the void fraction of solid phase at the location of fluid particle *a* is required. By applying Equation (49) to calculate the void fraction of solid phase at the location of fluid particle *a* and substituting this calculation back to Equation (51), we obtain:

$$n_a = 1 - \sum_{i=1}^{M} \frac{m_i}{\rho_i} n_i W_{ai} \tag{52}$$

where *M* is the total number of solid particles located within the support domain of fluid particle *a*. Owing to the fact that the void fraction of the solid phase is much less than 1, the above SPH approximation guarantees that the void fraction of fluid is always less than or equal to 1 for the flow inside and outside the porous medium, respectively.

3.3. SPH approximations of the continuity equations

As noted in Section 2.2, the continuity equation for the solid phase has been replaced by the void fraction equation and the SPH approximation for the void fractions have been presented in the previous section. This section will focus on the derivation of SPH approximations for the continuity equation of the fluid phase. By adopting the approach similar to that for the void fraction, the first term in the right hand-side of Equation (17) can be expanded as follows:

$$-\rho_w \left(\nabla \cdot \mathbf{v}_w\right) = -\left[\nabla \cdot \left(\rho_w \mathbf{v}_w\right) - \mathbf{v}_w \cdot \left(\nabla \rho_w\right)\right] \tag{53}$$

The SPH approximation of Equation (53) can be obtained by applying Equation (49) to each term on the right hand-side of this equation, resulting in:

$$\begin{aligned} -\left\{\rho_w \left(\nabla \cdot \mathbf{v}_w\right)\right\}_a &= -\sum_{b=1}^{N} \frac{\overline{m}_b}{\overline{\rho}_b} \left(\rho_b \mathbf{v}_b\right) \cdot \nabla_a W_{ij} + \sum_{b=1}^{N} \frac{\overline{m}_b}{\overline{\rho}_b} \left(\rho_b \mathbf{v}_a\right) \cdot \nabla_a W_{ab} \\ &= \sum_{b=1}^{N} \frac{\overline{m}_b}{n_b} \left(\mathbf{v}_a - \mathbf{v}_b\right) \cdot \nabla_a W_{ab} \end{aligned} \tag{54}$$

Similarly, by applying the same approach undertaken to obtain Equation (54), the SPH approximation of the second term in the right hand-side of Equation (17) is:

$$\left\{\frac{1-n_w}{n_w} \rho_w \left(\nabla \cdot \mathbf{v}_s\right)\right\}_a = \frac{1-n_a}{n_a} \sum_{b=1}^{N} \frac{\overline{m}_b}{n_b} \left(\mathbf{v}_a^s - \mathbf{v}_b^s\right) \cdot \nabla_a W_{ab} \tag{55}$$

where $\mathbf{v}_a^s$ and $\mathbf{v}_b^s$ are the velocity of solid phase at the location of fluid particle *a* and particle *b*, respectively. The velocity of solid phase at the location of fluid particle *a* is calculated using the following equation:

$$\mathbf{v}_s^a = \sum_{i=1}^{M} \frac{\overline{m}_i}{\overline{\rho}_i} \mathbf{v}_i W_{ai} \Big/ \sum_{i=1}^{M} \frac{\overline{m}_i}{\overline{\rho}_i} W_{ai} \tag{56}$$

Substituting Equations (54) and (55) into Equation (17) yields the following SPH approximation formulation for the mass balance of fluid phase in the deformable porous medium:

$$\frac{d\rho_a}{dt} = \sum_{b=1}^{N} \frac{\overline{m}_b}{n_b} \left(\mathbf{v}_a - \mathbf{v}_b\right) \cdot \nabla_a W_{ab} + \frac{1-n_a}{n_a} \sum_{b=1}^{N} \frac{\overline{m}_b}{n_b} \left(\mathbf{v}_a^s - \mathbf{v}_b^s\right) \cdot \nabla_a W_{ab} \tag{57}$$

3.4. SPH approximations of momentum equations for solid

The SPH approximation of the momentum equation for the solid phase in the deformable porous medium is presented in this section. The partial differential form of this equation was derived in Section 2.3, i.e. Equation (26), and is rearranged as follows:

$$\frac{d\mathbf{v}_s}{dt} = \frac{1}{\overline{\rho}_s}\nabla\cdot\boldsymbol{\sigma}' - \frac{1}{\overline{\rho}_s}n_s\nabla p_w + \mathbf{g} + \frac{\gamma_w n_w^2}{\overline{\rho}_s k}\left(\mathbf{v}_w - \mathbf{v}_s\right) \tag{58}$$

The first term in the right hand-side of Equation (58) can be rewritten as:

$$\left(\frac{1}{\overline{\rho}_s}\nabla\cdot\boldsymbol{\sigma}'\right)_i = \nabla\cdot\left(\frac{\boldsymbol{\sigma}'}{\overline{\rho}_s}\right)_i + \frac{\boldsymbol{\sigma}'}{\overline{\rho}_s^2}\cdot\left(\nabla\overline{\rho}_s\right)_i \tag{59}$$

Applying Equation (49) to the divergent terms in the right hand-side of Equation (58) yields:

$$\begin{aligned}\left(\frac{1}{\overline{\rho}_s}\nabla\cdot\boldsymbol{\sigma}'\right)_i &= \sum_{j=1}^{N}\frac{\overline{m}_j}{\overline{\rho}_j}\left(\frac{\boldsymbol{\sigma}'_j}{\overline{\rho}_j}\right)\cdot\nabla_i W_{ij} + \frac{\boldsymbol{\sigma}'_i}{\overline{\rho}_i^2}\sum_{j=1}^{N}\frac{\overline{m}_j}{\overline{\rho}_j}\left(\overline{\rho}_j\right)\cdot\nabla_i W_{ij} \\ &= \sum_{j=1}^{N}\overline{m}_j\left(\frac{\boldsymbol{\sigma}'_i}{\overline{\rho}_i^2} + \frac{\boldsymbol{\sigma}'_j}{\overline{\rho}_j^2}\right)\cdot\nabla_i W_{ij}\end{aligned} \tag{60}$$

The SPH approximation of the second term in the right hand-side of Equation (58) can be obtained using the same approach, leading to:

$$\left(\frac{n_s}{\overline{\rho}_s}\nabla p_w\right)_i = n_i\sum_{j=1}^{N}\overline{m}_j\left(\frac{p_{wi}}{\overline{\rho}_i^2} + \frac{p_{wj}}{\overline{\rho}_j^2}\right)\nabla_i W_{ij} \tag{61}$$

where p_{wi} and p_{wj} are the pore-fluid pressure of solid particles *i* and *j*, respectively. However, as proved by (Bui and Fukagawa, 2013), the use of Equation (61) or its alternative formulations resulted in numerical instability for soil particles located near the interface between submerged soil and water, unless a suitable dynamic boundary condition is enforced at this interface boundary. Treatments of such boundary condition require significant computational effort to search for soil particles located near the interface boundary between submerged soil and water. To avoid this expensive computational cost, a robust SPH approximation for the fluid pressure gradient proposed by (Bui and Fukagawa, 2013), which automatically accounts for the dynamic boundary condition between submerged solid phase and water, is adopted in this work. Accordingly, the second term in the right hand-side of Equation (58) can be approximated using the following equation:

$$\left(\frac{1}{\overline{\rho}_s}n_s\nabla p_w\right)_i = n_i\sum_{j=1}^{N}\overline{m}_j\left(\frac{p_{wi} - p_{wj}}{\overline{\rho}_i\overline{\rho}_j}\right)\nabla_i W_{ij} \tag{62}$$

where p_{wi} is the pore-water pressure at the location of a soil particle *i* and is calculated by taking the integration of the pore-water pressure from surrounding water particles located within the support domain of the soil particle *i* as follows:

$$p_{wi} = \sum_{a=1}^{M}\frac{\overline{m}_a}{\overline{\rho}_a}p_a W_{ia} \Big/ \sum_{a=1}^{M}\frac{\overline{m}_a}{\overline{\rho}_a}W_{ia} \tag{63}$$

The SPH approximation of the last term in the right hand-side of Equation (58), i.e. seepage force per unit volume, is quite straight forward as it does not involve any spatial derivative. However, it is noticed that the water velocity ($\mathbf{v}_w$) in this formulation should be interpreted as the water velocity at the location of soil particle (not the velocity of water particle). This velocity is denoted as $\mathbf{v}_w^s$ and can be obtained using the similar approach undertaken to evaluate the pore-water pressure at the location of soil particles, i.e. Equation (63). Accordingly, the seepage force term can be approximated using the following equation:

$$\left\{\frac{\gamma_w n_w^2}{\overline{\rho}_s k}\left(\overline{\mathbf{v}}_w-\mathbf{v}_s\right)\right\}_i=\frac{\gamma_w \overline{n}_{ai}^2}{\overline{\rho}_i k_i}\left(\sum_{a=1}^{M}\frac{\overline{m}_a}{\overline{\rho}_a}\left(\mathbf{v}_a^s-\mathbf{v}_i\right)W_{ia}\right)\Bigg/\sum_{a=1}^{M}\frac{\overline{m}_a}{\overline{\rho}_a}W_{ia} \tag{64}$$

where $\overline{n}_{ai}$ is the arithmetic averages of the void fraction of soil and water particles.

Alternatively, a more formal form of the seepage force term, which conserves both linear and angular momentums, can be obtained by smoothing with the kernel employing the following integral interpolation (Bui et al., 2007; Monaghan, 1997):

$$\frac{\gamma_w n_w^2}{\overline{\rho}_s k}\left(\mathbf{v}_w(\mathbf{r})-\mathbf{v}_s(\mathbf{r})\right)=\vartheta\frac{\gamma_w n_w^2}{\overline{\rho}_s k}\int\left\{\frac{\Delta\mathbf{v}'\cdot\Delta\mathbf{r}'}{\left(\Delta\mathbf{r}'\right)^2+\eta^2}\right\}\Delta\mathbf{r}'W\left(\mathbf{r}'-\mathbf{r}\right)d\mathbf{r}' \tag{65}$$

where:

$$\Delta\mathbf{v}'=\mathbf{v}_w(\mathbf{r})-\mathbf{v}_s(\mathbf{r}') \qquad \text{and} \qquad \Delta\mathbf{r}'=\mathbf{r}-\mathbf{r}' \tag{66}$$

In Equation (65), η^2 is a clipping constant (taken as $0.001h^2$), which prevents singularities when a water particle and a soil particle coincides, and ϑ is a constant equal to the inverse of the number of dimensions, i.e. $\vartheta=1/2$ for two-dimension and $\vartheta=1/3$ for three-dimension. The clipping constant is effective only when the distance between two SPH particles is less than $0.1h$. In reality, such a close distance (i.e. less than $0.1h$) should be avoided in SPH simulations as it reduces the accuracy of SPH approximation. Nevertheless, when the distance between two particles is much larger than $0.1h$, which is the case of our simulations, the inclusion of this parameter introduces negligible errors when the clip constant is taken to be less than or equal to $0.001h^2$. In the subsequent sections, this clip constant will be adopted whenever required to avoid numerical singularities in SPH simulations when two particles are getting too close to each other.

The SPH approximation of Equation (65) for a soil particle is obtained by replacing the integral by a sum over water particles located within the supporting domain of the soil particle:

$$\left\{\frac{\gamma_w n_w^2}{\overline{\rho}_s k}\left(\overline{\mathbf{v}}_w(\mathbf{r})-\mathbf{v}_s(\mathbf{r})\right)\right\}_i=\vartheta\frac{\gamma_w}{k_i}\sum_{a=1}^{M}\frac{\overline{m}_a\overline{n}_{ai}^2}{\overline{\rho}_i\overline{\rho}_a}\left\{\frac{\mathbf{v}_{ia}\cdot\mathbf{r}_{ia}}{\left|\mathbf{r}_{ab}\right|^2+\eta^2}\right\}\mathbf{r}_{ia}W_{ia} \tag{67}$$

Equation (67) shows that the seepage force per unit volume acts like a repulsive force when particles are approaching, and if they are receding, it acts like an attractive force. This force acts along the line connecting two particles, and thus the conservation of linear and angular momentum is guaranteed. In this paper, Equation (67) is used rather than Equation (64). Both formulations yield similar results according to our numerical tests; however, in our experience Equation (67) is more robust because it requires no additional computational cost to calculate soil velocity at the location of water particle.

Finally, substituting Equations (60), (62) and (67) into Equation (58) yields the following the SPH approximation for the momentum equation of a soil particle in the deformable porous medium:

$$\begin{aligned}\frac{d\mathbf{v}_i}{dt}=&\sum_{j=1}^{N}\overline{m}_j\left(\frac{\boldsymbol{\sigma}_i'}{\overline{\rho}_i^2}+\frac{\boldsymbol{\sigma}_j'}{\overline{\rho}_j^2}+\mathbf{C}_{ij}\right)\cdot\nabla_i W_{ij}-n_i\sum_{j=1}^{N}\overline{m}_j\left(\frac{p_{wi}-p_{wj}}{\overline{\rho}_i\overline{\rho}_j}\right)\nabla_i W_{ij}\\&+\vartheta\frac{\gamma_w}{k_i}\sum_{a=1}^{M}\frac{\overline{m}_a\overline{n}_{ai}^2}{\overline{\rho}_i\overline{\rho}_a}\left\{\frac{\mathbf{v}_{ia}\cdot\mathbf{r}_{ia}}{\left|\mathbf{r}_{ai}\right|^2+\eta^2}\right\}\mathbf{r}_{ia}W_{ia}+\mathbf{g}_i\end{aligned} \tag{68}$$

where $\mathbf{C}_{ij}$ is a stabilisation term utilised to remove the stress fluctuation and tensile instability in soils (Bui et al., 2008; Bui et al., 2011a). Equation (68) can be solved using the standard leap-frog integration scheme if the effective stress tensor and pore-water pressure are known. Thus, it is

necessary to establish SPH equations for these quantities.

3.5. SPH approximations of momentum equation for fluid phase

As discussed in Section 2.5, the two-step prediction-correction time integration scheme is chosen to advance the velocity and position of the water phase. Thus, the SPH approximation for the momentum equation of the water phase will be derived in accordance with the predictor-corrector scheme, i.e. Equations (37-44), using the similar approach undertaken to derive the momentum equation for the solid phase. The momentum equation of the fluid phase is rewritten as follows:

$$\frac{d\mathbf{v}_w}{dt} = -\frac{1}{\rho_w}\nabla p_w + \mathbf{g} - \frac{\gamma_w n_w^2}{\bar{\rho}_w k}\left(\mathbf{v}_w - \mathbf{v}_s\right) \tag{69}$$

The solution of the above equation in the two-step prediction-correction time integration requires the approximation of the following equations:

$$\mathbf{v}_w^* = \mathbf{v}_w^t + \left[\mathbf{g} - \frac{\gamma_w n_w^2}{k}\left(\mathbf{v}_w - \mathbf{v}_s\right)\right]\Delta t \tag{70}$$

$$\mathbf{v}_w^{t+1} = \mathbf{v}_w^* - \frac{1}{\rho_w^*}\nabla p_w^{t+1}\Delta t \tag{71}$$

$$\nabla\cdot\left(\frac{1}{\rho^*}\nabla p_w^{t+1}\right) = \frac{\rho_w^0 - \rho_w^*}{\rho_w^0 \Delta t^2} - \frac{1-n_w}{n_w \Delta t}\nabla\cdot\mathbf{v}_s \tag{72}$$

In the first prediction step, the pressure gradient is ignored and only the last two terms in the right hand-side of Equation (70) are used to predict a temporal velocity ($\mathbf{v}^*$) as shown in Equation (70). Thus, SPH approximation of the seepage force term is required. By adopting the similar approach used for the approximation of the seepage force acting on soil particle due to the water flow, two alternative SPH approximations of the seepage drag force acting on water particle (a) due to surrounding soils (i) can be obtained as follows:

$$\left\{\frac{\gamma_w n_w^2}{\bar{\rho}_s k}\left(\mathbf{v}_w - \mathbf{v}_s\right)\right\}_a = \frac{\gamma_w \bar{n}_{ai}^2}{\bar{\rho}_i k_i}\left(\sum_{i=1}^{N}\frac{\bar{m}_i}{\bar{\rho}_i}(\mathbf{v}_a - \mathbf{v}_i^w)W_{ia}\right)\Big/\sum_{i=1}^{N}\frac{\bar{m}_i}{\bar{\rho}_i}W_{ia} \tag{73}$$

$$\left\{\frac{\gamma_w n_w^2}{\bar{\rho}_w k}\left(\mathbf{v}_w - \mathbf{v}_s^w\right)\right\}_a = \vartheta\frac{\gamma_a}{k_i}\sum_{i=1}^{M}\frac{\bar{m}_i \bar{n}_{ai}^2}{\bar{\rho}_a \bar{\rho}_i}\left\{\frac{\mathbf{v}_{ai}\cdot\mathbf{r}_{ai}}{|\mathbf{r}_{ai}|^2 + \eta^2}\right\}\mathbf{r}_{ai}W_{ai} \tag{74}$$

The second form of the seepage force is selected for consistency with the recommendation for the solid phase. Accordingly, the intermediate temporal velocity of the fluid phase inside the porous medium, i.e. Equation (70), is updated using the following equation:

$$\mathbf{v}_a^* = \mathbf{v}_a^t + \left[\mathbf{g} - \vartheta\frac{\gamma_a}{k_i}\sum_{i=1}^{M}\frac{\bar{m}_i \bar{n}_{ai}^2}{\bar{\rho}_a \bar{\rho}_i}\left\{\frac{\mathbf{v}_{ai}\cdot\mathbf{r}_{ai}}{|\mathbf{r}_{ai}|^2 + \eta^2}\right\}\mathbf{r}_{ai}W_{ai}\right]\Delta t \tag{75}$$

On the other hand, for the fluid flow outside the porous medium, the seepage force vanishes and the water phase becomes inviscid fluid. However, to simulate more realistic behaviour of the fluid flow, viscosity should be considered for the motion of the fluid phase. Accordingly, for the water flow outside the porous medium, the standard viscosity formulation commonly used for free-surface flow (Shao and Lo, 2003) is adopted and the intermediate temporal velocity of the fluid flow outside the porous medium is:

$$\mathbf{v}_a^* = \mathbf{v}_a^t + \left[\mathbf{g} - \sum_{b\neq a}^{N} \frac{\overline{m}_b}{n_b} \frac{4(\nu_a + \nu_b)}{(\rho_a + \rho_b)^2} \frac{\mathbf{v}_{ab}^t \cdot \mathbf{r}_{ab}}{|\mathbf{r}_{ab}|^2 + \eta^2} \nabla_a W_{ab} \right] \Delta t \tag{76}$$

where ν_a and ν_b are the kinematic viscosity of water particle a and b, respectively.

Next, the SPH approximation for the gradient term of the pore-water pressure is needed to adjust the velocity of water particles in the correction step; see Equation (71). The gradient of the pore water pressure can be written as follows:

$$\left(-\frac{1}{\rho_w^*} \nabla p_w^{t+1} \right)_a = -\nabla \left(\frac{p_w^{t+1}}{\rho_w^*} \right)_a - \left(\frac{p_w^{t+1}}{\rho_w^{2*}} \nabla \rho_w^* \right)_a \tag{77}$$

Applying Equation (49) to the gradient terms in the right hand-side of Equation (77) yields the following SPH approximation for the pressure gradient of a certain fluid particle *a*:

$$\left(-\frac{1}{\rho_w^*} \nabla p_w^{t+1} \right)_a = -\sum_{b=1}^{N} \frac{\overline{m}_b}{\overline{\rho}_b} \left(\frac{p_a^{t+1}}{\rho_a^*} + \frac{p_b^{t+1}}{\rho_b^*} \right) \nabla_a W_{ab} \tag{78}$$

Here, we have adopted the assumption of $\rho_a^* = \rho_b^*$ to simplify the approximation, taking into consideration the incompressible condition of the fluid flow.

Finally, to evaluate the pressure gradient in Equation (78), one needs to solve the pressure Poisson's equation (72) that involves the Laplacian operator and divergence of the velocity which need to be approximated in the SPH framework. The Laplacian operator can be formulated in a standard way using the combination of the divergence and gradient operators of SPH formulations. However, it has been found that the resulting second derivative of the kernel is very sensitive to particle disorder and could easily lead to pressure instability and decoupling in the computation due to the co-location of the velocity and pressure (Shao and Lo, 2003). In this work, the same approach suggested by (Shao and Lo, 2003) is adopted. The approach is a hybrid of a finite difference approximation and the standard SPH approximation for the first derivative. By considering the Taylor series expansions of the pressure and the density, taking the integral interpolation of the Taylor expansion functions and finally adopting the standard SPH approximation for the gradient term, the following SPH approximation for the pressure Poisson equation can be derived:

$$\nabla \cdot \left(\frac{1}{\rho^*} \nabla p^{t+1} \right)_a = \sum_{b\neq a}^{N} \frac{\overline{m}_b}{n_b} \frac{8}{\left(\rho_a^* + \rho_b^*\right)^2} \frac{\left(p_a^{t+1} - p_b^{t+1}\right) \mathbf{r}_{ab} \cdot \nabla_a W_{ab}}{\mathbf{r}_{ab}^2 + \eta^2} \tag{79}$$

The divergence of the velocity can be approximated straightforwardly using the same approach employed to derive the continuity equation, which yields:

$$\left(\frac{1 - n_w}{n_w \Delta t} \nabla \cdot \mathbf{v}_s \right)_a = \frac{1 - n_a}{n_a \Delta t} \sum_{b=1}^{N} \frac{\overline{m}_b}{\overline{\rho}_b} \left(\mathbf{v}_a^s - \mathbf{v}_b^s \right) \cdot \nabla_a W_{ab} \tag{80}$$

where $\mathbf{v}_a^s$ and $\mathbf{v}_b^s$ are the velocity of solid phase at the location of fluid particle *a* and particle *b*, which are evaluated using Equation (56). Substituting Equation (70-71) into Equation (72) yields the following coupled pressure Poisson's equation for the fluid flow through the deformable porous medium:

$$\sum_{b\neq a}^{N} \frac{\overline{m}_b}{n_b} \frac{8}{\left(\rho_a^* + \rho_b^*\right)^2} \frac{\left(p_a^{t+1} - p_b^{t+1}\right) \mathbf{r}_{ab} \cdot \nabla_a W_{ab}}{\mathbf{r}_{ab}^2 + \eta^2} = \frac{\rho_a^0 - \rho_a^*}{\rho_a^0 \Delta t^2} + \frac{1 - n_a}{n_a \Delta t} \sum_{b=1}^{N} \frac{\overline{m}_b}{\overline{\rho}_b} \left(\mathbf{v}_a^s - \mathbf{v}_b^s \right) \cdot \nabla_a W_{ab} \tag{81}$$

Compared to the free-surface incompressible fluid flows or any previous two-phase coupled models following the original two-phase flow framework proposed by (Bui et al., 2007), the current framework is novel in the sense that an additional source term due to solid matrix deformations is taken into consideration when solving the pressure Poisson's equation for the pore-fluid. Furthermore, the variation of void fractions is fully taken into consideration in deriving the governing equations for the two-phase mixture. For the case of a rigid porous media, the additional source term due to soil deformation vanishes and Equation (81) returns to the normal pressure Poisson's equation for incompressible flow. Equation (81) can be solved efficiently using a precondition conjugate gradient iterative method (Shao and Lo, 2003) that involves solving large sparse systems of linear equations for large scale applications, which is not straightforward. Alternatively, a rather simpler approach which uses a fully explicit integration scheme (Nomeritae et al., 2016) can be applied to solve the above pressure Poisson's equation in a more efficient way. The latter approach is adopted in the current work based on its merits, and the water pressure of a certain water particle *a* is calculated by rearranging Equation (81) in the following manner:

$$p_a^{t+1} = \frac{B_a + \sum_{b=1}^{N} A_{ab} p_b^{t+1}}{\sum_{b=1}^{N} A_{ab}} \tag{82}$$

where A_{ab} and B_a are defined as follows:

$$A_{ab} = \sum_{b \neq a}^{N} \frac{\overline{m}_b}{n_b} \frac{8}{\left(\rho_a^* + \rho_b^*\right)^2} \frac{\mathbf{r}_{ab} \cdot \nabla_a W_{ab}}{(\mathbf{r}_{ab}^2 + \eta^2)} \tag{83}$$

$$B_a = \frac{\rho_a^0 - \rho_a^*}{\rho_a^0 \Delta t^2} + \frac{1 - n_a}{n_a \Delta t} \sum_{j=1}^{M} \frac{\overline{m}_j}{\overline{\rho}_j} \left(\overline{\mathbf{v}}_{ia} - \overline{\mathbf{v}}_{ja}\right) \cdot \nabla_a W_{ab} \tag{84}$$

For a small time increment of the explicit scheme, the value of p_b^{t+1} can be assumed to be equal to p_b^t, thus there is no need to perform numerical iteration for the solution of Equation (81). Accordingly, the pressure of each fluid particle can be explicitly computed in time using the following simplified equation:

$$p_a^{t+1} = \frac{B_a + \sum_{b=1}^{N} A_{ab} p_b^{t}}{\sum_{b=1}^{N} A_{ab}} \tag{85}$$

Finally, at the end of each round of computation, the density of each fluid particle is forced to its initial density and thus the incompressible condition of the fluid phase is also further enforced after each time step. The recent numerical tests for the fluid flow presented in (Nomeritae et al., 2016) show that the proposed explicit incompressible SPH method (EISPH) is four times as fast as the δ-SPH (Antuono et al., 2010), which is one of the most advanced weakly compressible SPH models, while yielding the same level of accuracy. For further details of this approach, we refer readers to prior publication (Nomeritae et al., 2016).

3.6. SPH approximation of soil constitutive relation

In the SPH framework, the explicit expression of the time derivative of a stress-strain relation is required for the numerical solution. By further expanding Equations (28) and (29), enforcing the consistency of the yield function and applying the SPH approximation, the following explicit expression of the stress rate tensor at a soil particle *i* can be obtained (Bui and Fukagawa, 2013):

$$\frac{d\sigma_i'^{\alpha\beta}}{dt} = \sigma_i'^{\alpha\gamma}\dot{\omega}_i^{\beta\gamma} + \sigma_i'^{\gamma\beta}\dot{\omega}_i^{\alpha\gamma} + 2G_i\dot{e}_i^{\alpha\beta} + K_a\dot{\varepsilon}_i^{\gamma\gamma}\delta_i^{\alpha\beta} - \dot{\lambda}_i\left[3K_i\alpha_{\psi i}\,\delta^{\alpha\beta} + (G_i/\sqrt{J_{2i}})_i\, s_i'^{\alpha\beta}\right] \quad (86)$$

where G_i is the shear modulus, K_i is the bulk modulus, $\dot{\varepsilon}_i^{\alpha\beta}$ and $\dot{\omega}_i^{\alpha\beta}$ are the strain rate spin rate tensors, respectively; $\dot{e}_a^{\alpha\beta} = \dot{\varepsilon}_a^{\alpha\beta} - \frac{1}{3}\dot{\varepsilon}_a^{\gamma\gamma}\delta^{\alpha\beta}$ is the deviatoric shear strain rate tensor, $s_i'^{\alpha\beta}$ is the deviatoric shear stress tensor and $\dot{\lambda}_i$ is the rate of plastic multiplier computed by:

$$\dot{\lambda}_i = \frac{3\alpha_{\phi i}K_i\dot{\varepsilon}_i^{\gamma\gamma} + (G_i/\sqrt{J_{2i}})s_i'^{\alpha\beta}\dot{\varepsilon}_i^{\alpha\beta}}{9\alpha_{\phi i}K_i\alpha_{\psi i} + G_i} \quad (87)$$

The strain rate and spin rate tensors are calculated by:

$$\dot{\varepsilon}_i^{\alpha\beta} = \frac{1}{2}\left[\sum_{j=1}^{N}\frac{\overline{m}_j}{\overline{\rho}_j}(\dot{u}_j^{\alpha} - \dot{u}_i^{\alpha})\nabla_i W_{ij} + \sum_{j=1}^{N}\frac{\overline{m}_j}{\overline{\rho}_j}(\dot{u}_j^{\beta} - \dot{u}_i^{\beta})\nabla_i W_{ij}\right] \quad (88)$$

$$\dot{\omega}_i^{\alpha\beta} = \frac{1}{2}\left[\sum_{j=1}^{N}\frac{\overline{m}_j}{\overline{\rho}_j}(\dot{u}_j^{\alpha} - \dot{u}_i^{\alpha})\nabla_i W_{ij} - \sum_{j=1}^{N}\frac{\overline{m}_j}{\overline{\rho}_j}(\dot{u}_j^{\beta} - \dot{u}_i^{\beta})\nabla_i W_{ij}\right] \quad (89)$$

The validations of the above soil model within the SPH framework has been extensively documented in previous works (Bui and Fukagawa, 2013; Bui et al., 2008; Bui et al., 2011a; Bui et al., 2014; Chen and Qiu, 2012; Deb and Pramanik, 2013; Nguyen et al., 2017), in which excellent agreements between SPH solutions and finite element as well as experiments have been achieved. To avoid repetition, we refer readers to previous publications for details of the validation process and SPH performance for elaso-plastic computation.

3.7. Calculation of the degree of saturation using SPH approximation

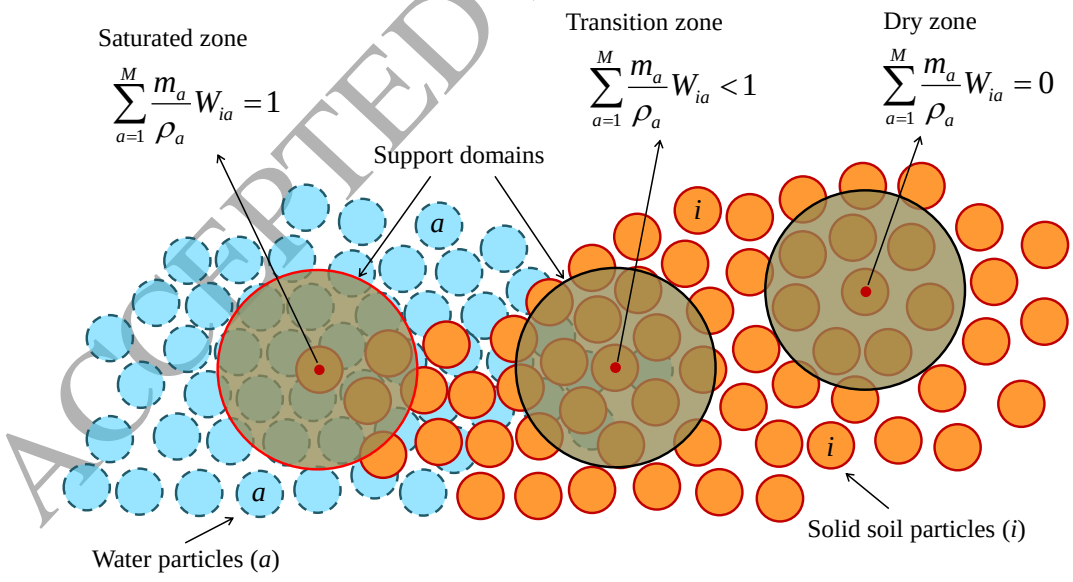

Figure 2: Schematic view of water seeping through porous media

In soil mechanics, soil is said to be fully saturated if the degree of saturation is $S_r = 1$, dry if the degree of saturation is $S_r = 0$, and unsaturated if the degree of saturation is $0 < S_r < 1$. Dealing with unsaturated soil behaviour is a quite complicated task and is beyond the scope of this paper. Here, we

mainly consider two conditions of soil, dry and fully saturated conditions. There is also a zone between dry and saturated soil which calls transition zone rather than unsaturated zone. Figure 2 shows a schematic diagram which outlines the progress of water seeping through the porous media. It can be seen that when a soil particle is fully submerged in water, its support domain is fully filled by water particles. On the other hand, those located far away from water particles in the dry zone have no water particles in their supporting domain. For those solid soil particles located in the transition zone, part of their support domain is filled with water particles, while the other part is filled with solid particles. The above soil condition can be effectively modelled by taking advantage of the SPH approximation, Equation (48). Accordingly, the degree of saturation of a soil particle *i* in the current computational framework can be estimated using the following equation:

$$s_{ri} = \sum_{a=1}^{M} \frac{\overline{m}_a}{\overline{\rho}_a} W_{ia} \tag{90}$$

where the summation has been taken over water particles. Owing to the nature of SPH summation approximation, Equation (90) will result in $s_r \approx 1$ for soil particles whose supporting domain are fully filled by water particles and $s_r = 0$ for soil particles whose their support domain has no water particles. On the other hand, for soil particles located in the transition zone, because of the truncation of the kernel function, Equation (90) will result in a degree of saturation of less than unity. The range of the transition zone above the saturated soil domain depends on the smoothing length of the kernel function.

3.8. Coupled SPH algorithm for the fluid-solid mixture

The coupled SPH algorithm for the fluid-solid mixture requires information from two phases to be exchanged during the computational process. The outline of the proposed coupled algorithm is shown in Figure 3 and details are explained below:

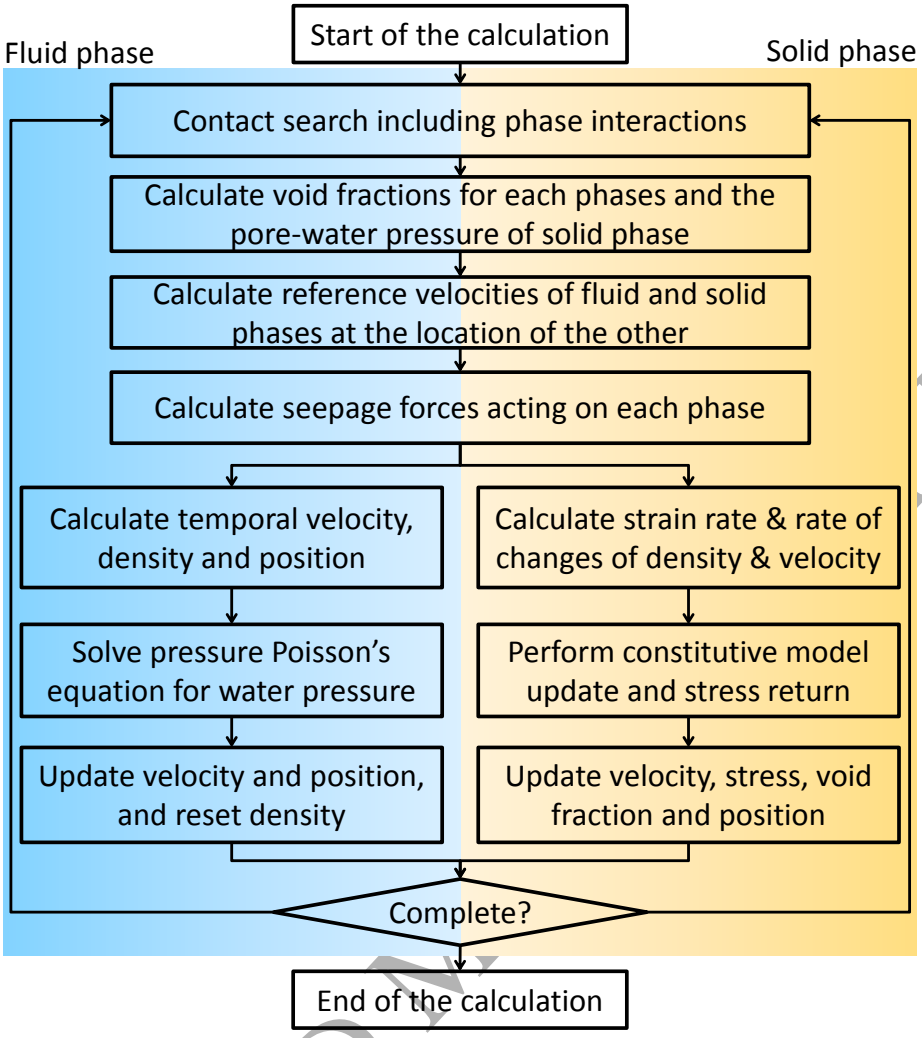

Figure 3: SPH computational procedure to solving coupled fluid-solid mixtures

i) At the start of the computational procedure, both fluid and solid particles are generated and each of which carries their own physical properties and field variables. The procedure for searching contact interaction will be then undertaken to determine interaction pairs of particles in the same phase and from different phases. The interaction pair is only formed if the distance between two particles is less than the radius of the supporting domain, which is equal to 2*h* in this work.

ii) Next, based on the contact information, the void fraction of fluid particles, reference velocities of each phase particles at the location of the other, and the pore-water pressure at the location of solid particles are calculated. This information is then used in the governing equations of each phase to consider the coupling effects in the seepage force and pressure Poisson's equation.

iii) Finally, the governing equations of each phase will then be solved taking into consideration coupling terms calculated in Step ii) and field variables of each phase will be updated at the end of each time step.

4. TREATMENT OF BOUNDARY CONDITIONS

Despite its advantage in handling large deformation and moving interface problems, the treatment of solid or prescribed boundary conditions in the SPH method is not straightforward. This is because when a particle (or material point) approaches the solid boundaries of a problem domain, the supporting domain of a SPH kernel function will be truncated by the boundary, and thus SPH approximations are no longer accurate. Accordingly, the treatment of SPH boundary conditions has been an ongoing concern for an accurate and successful implementation of the SPH approach. In this work, two different types of boundary conditions are required, one for the solid porous medium phase and the other for the fluid phase. The boundary conditions for the deformable porous medium generally consist of full-fixity and free-roller wall boundaries, which can be modelled using fixed boundary particles (Bui et al., 2008) and ghost particles (Libersky et al., 1993), respectively.

On the other hand, three types of boundary conditions for the fluid phase are required in this work. These include impermeable rigid wall boundary, free-surface boundary and water inlet boundary. The impermeable rigid wall boundaries of the fluid phase can be simulated following the approach proposed by (Shao and Lo, 2003), in which two set of fixed boundary particles are used to model the wall boundary (wall particles and dummy particles). The pressure Poisson's Equation (85) is solved on the wall particles and then copying to the dummy particles to satisfy the Neumann boundary condition, while the velocities of both wall and dummy particles are set to zero to represent the non-slip boundary conditions. In addition, to prevent fluid particles moving too close to the solid walls for simulations with long physical time problem, a repulsive force following the Lennard-Johns form (Monaghan, 1994) is applied to fluid particles that move close to the wall boundary.

The free-surface boundary condition for the fluid phase requires a zero pressure value for those particles located on the free-surface. In this work, a particle is regarded as a free-surface particle if its initial density fluctuation exceeds 1% below that of the inner fluid. A Dirichlet boundary condition of zero pressure is then given to this particle during the computation. Finally, the inlet boundary condition for incoming flow discharges through permeable porous media (see Section 5.3) is modelled following the original work proposed by (Lastiwka et al., 2009), in which an inflow zone is defined outside the flow domain by extruding the inlet boundary in the upstream direction. The length of the inflow zone must be at least equal to the size of the kernel supporting domain used in the SPH simulation. Particles inside the inflow zone will move with a prescribed velocity, while leaving pressure and density to be determined by the information propagated from the fluid domain. During the computation, for any particle that moves out of the inflow zone at the boundary between the fluid domain and the inflow zone, a new particle will be created at the inlet upstream to compensate for the particle loss.

5. VALIDATIONS AND APPLICATION OF THE PROPOSED MODEL

In this section, a series of benchmark tests are performed to validate the proposed SPH framework. In the first test, a simple problem of a fully submerged homogenous soil medium subjected to a gravity load is simulated. The numerical solutions obtained are validated against the analytical solutions for the hydrostatic water pressure and soil stresses. The second test concerns a transient seepage flow through a linear elastic isotropic homogenous soil embankment, in which the solutions of the flow properties and the distribution of pore-water pressure obtained with the proposed framework are compared with FEM solutions. In the third test, the proposed SPH framework is validated against several experiments of water flows through rockfill dams performed in the XPRESS and E-DAMS projects (Larese, 2012). In these experiments, different flow discharges were imposed and corresponding evolutions of the pressure head were recorded; they will be used for the validation of the proposed framework. Finally, the proposed SPH framework is applied to simulate a laboratory scale experiment of a seepage flow induced large deformation and failure of an embankment conducted by the first author.

5.1. Verification with analytical solutions for initial in-situ stresses

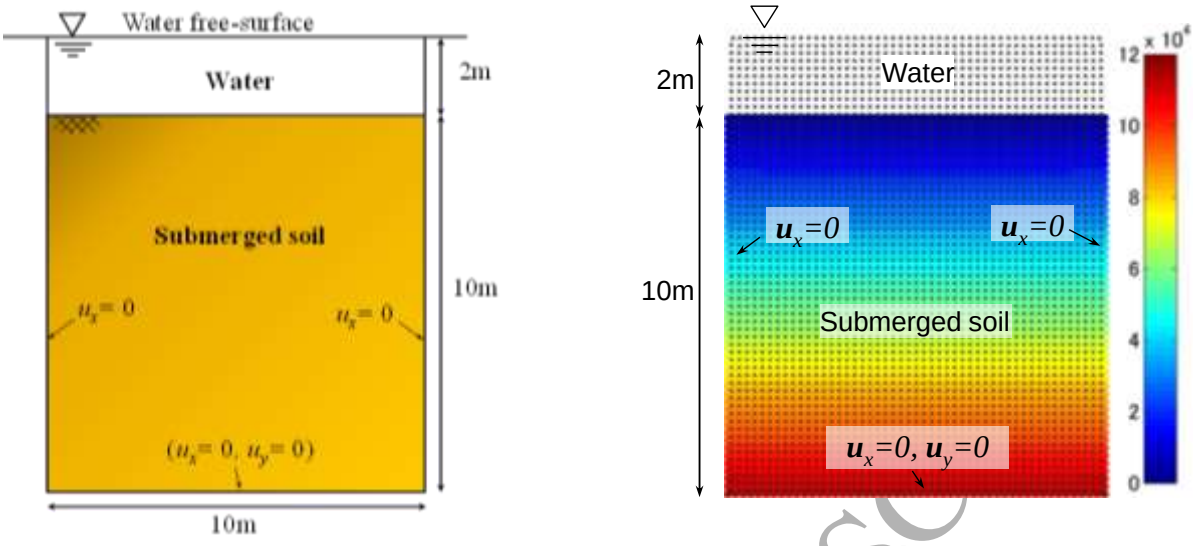

Figure 4: Model test of a fully submerged soil medium in a still water body.

A plane-strain problem of a saturated soil medium submerged in water is considered in this section. The main purpose of this example is to examine the initial in-situ stress distribution inside the undisturbed soil medium when the velocity of the water phase is assumed to be zero. The geometry and boundary conditions of the saturated soil medium are taken similar to (Bui and Fukagawa, 2013) as shown in Figure 4a. However, in contrast to (Bui and Fukagawa, 2013), both the soil and water are modelled herein by the SPH method. The soil is assumed to be an elastic isotropic homogenous material with the following properties: Young's modulus E = 100 MPa, Poisson's ratio ν = 0.3 and the dry unit weight γ_s = 26 kN/m^3. The unit weight of water is γ_w = 9.81 kN/m^3. The porosity, i.e. void fraction of water, is kept constant at n = 0.3 as this example deals with a still water body. In the SPH simulation, the model test is discretised using 5500 particles (3000 particles for water body and 2500 particles for soil medium) arranged in a regular lattice with a uniform spacing of 0.2 m and a smoothing length of h = 0.24 m. Boundary conditions are treated as follows (see Section 4): for the soil medium, fixed boundary particles are used to model the full-fixity at the bottom, while ghost particles satisfying the free-roller condition are assigned to vertical sides; for the water body, wall and dummy particles were used to enforce the no-slip boundary condition. Initially, the soil stresses are set to zero, while the water pressure is set to the hydrostatic condition. The gravity loading is then applied in a single increment to obtain the initial in-situ stress distributions in the soil medium. In order to avoid stress fluctuations from the sudden application of self-weight loading and the zero-energy mode in SPH, the damping force suggested by (Bui and Fukagawa, 2013) is adopted for soil particles with the damping coefficient taken to be ξ = 0.02; no damping force is applied to the water phase. In addition, for the purpose of validating the initial in-situ stresses under the quasi-static condition, the seepage force is deactivated in the current simulation. No additional efforts are taken to enforce the dynamic boundary condition on the interface between the submerged soil and water.

Figure 4b shows the colour plots of the in-situ effective vertical stress distribution in the soil medium using the proposed two-phase SPH framework. A smooth stress profile is achieved within the soil medium, suggesting that the explicit ISPH solution for the pore-fluid is stable. The effective vertical stress at the ground surface is zero and this corresponds to the fact that the total vertical stress is equal to the weight of the free standing surface. Similar to the finding reported in (Bui and

Fukagawa, 2013), although no additional computational effort is taken to apply forces due to surcharge pressure to particles located at the interface between soil and water, the coupled numerical solution remains stable thanks to the robust inclusion of the pore water pressure into soil particles using Equation (62). On the other hand, a problem of particles expelling from the ground surface is observed if Equation (61) is used to approximate the gradient of the pore-water pressure. The accuracy of the proposed two-phase SPH framework is examined in Figure 5 by comparing the results predicted by the SPH simulations with the analytical solutions for the horizontal stresses, vertical stresses and pore-water pressure. In the SPH simulation, the soil stresses and pore-water pressure are computed at the vertical central line of the soil medium with an interval of 1 m from the ground surface to the base. It can be seen that the current numerical model can predict well the initial in-situ stresses and the pore-water pressure. At the ground surface, the effective stresses are zero and the total stresses are equal to the weight per unit area of the free-standing water. At other locations, the numerically calculated stresses agree well with the analytical results. The hydrostatic pore-water pressure is also correctly predicted using the explicit-ISPH model. The good agreement between SPH computation and theoretical solutions confirmed that the coupling procedure in the two-phase SPH framework works well.

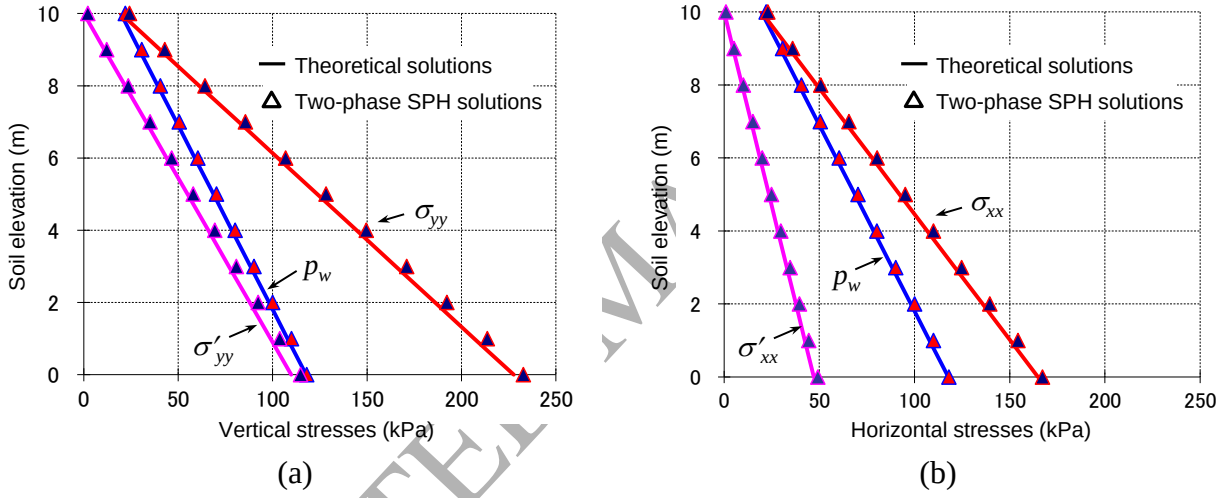

Figure 5: Comparisons of the stress profiled between the SPH and theoretical solutions.

5.2. Verification with FEM solutions for seepage flow behaviour

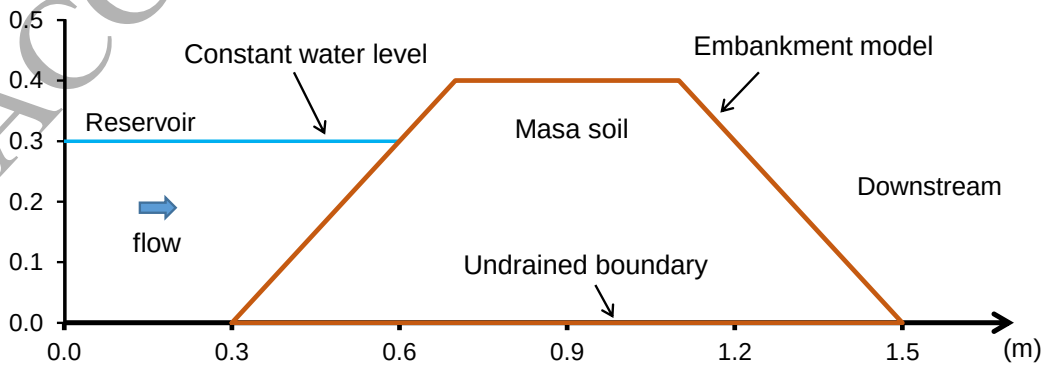

Figure 6: Initial geometry and setting conditions of an embankment.

In this second test, the transient seepage flow through an elastic isotropic homogeneous soil embankment is considered. The solutions of the flow properties and the distribution of pore water pressure obtained with the two-phase SPH framework are compared with the steady-state solutions obtained by the PLAXIS finite element (FE) commercial software package. For the purpose of testing the accuracy and performance of the two-phase SPH model for the seepage flow through the embankment, the soil material is assumed to be elastic to avoid the failure of the embankment, which could not be handled by FEM.

The geometry and dimensions of the embankment are shown in Figure 6. The embankment model is 40 cm high with 40 cm top width and both the upstream and downstream slopes are 1:1. The soil properties are: Young's modulus E = 3.0 MPa, Poisson's ratio υ = 0.3, the dry unit weight γ_s = 25.5 kN/m^3, initial permeability 1.1×10^{-4} m/s and initial porosity 0.4. In the PLAXIS FE-model, the embankment is discretised using 1568 15-node triangular elements, which correspond to 18816 materials points (i.e. Gauss points). The constant flux equivalent to the water head level of 30 cm is applied to the upstream slope of the embankment in a form of the linear increasing head pressure on the side boundary. In the SPH model, on the other hand, the embankment is modelled with 3160 particles arranged in a regular lattice with an initial spacing of 1 cm and the smoothing length is 1.2 cm. To model the incoming water flow, SPH particles representing the water phase are continuously generated and dropped gently from the left reservoir during the computational process. It takes approximately 30 seconds to reach the required water level of 30 cm. In order to maintain the required water level in the reservoir, a computational routine is developed to generate water particles if the maximum water level in the reservoir is less than 30 cm. Water particles that move out of the right boundary are deleted from the computation to save the computational cost. The initial in-situ stress condition of the embankment in both FEM and SPH simulations is obtained by applying gravity loading (Bui and Fukagawa, 2013).

Figure 7 shows the progressive development of the saturated zone due to the seepage flow and the corresponding pore-water pressure distribution inside the embankment. On the left side of the figure, the orange colour represents the fully saturated zone where S_r = 1, whereas the blue colour indicates the fully dry zone where S_r = 0. There is a transition zone in which the degree of saturation is in a range of S_r = 0.0-1.0. It should be noted that this is a numerically-generated zone which is due to the truncation of the kernel function at the boundary between the saturated and dry zone in the SPH approximation of the degree of saturation (see Section 3.7). On the right side, the zero-pressure head line is redrawn by connecting all water particles located on the free-surface inside the embankment. It is noticed that there is also a thin zone of 2h wide above these lines in which the pore-water pressure value is not zero. This is again a numerically-generated value due to the truncation of the kernel function when calculating the pore-water pressure for soil particles. In fact, the kernel truncation error in SPH is an interesting feature which can be very useful for the modelling of unsaturated soils whereas there is always a transient zone between saturated and dry soils.

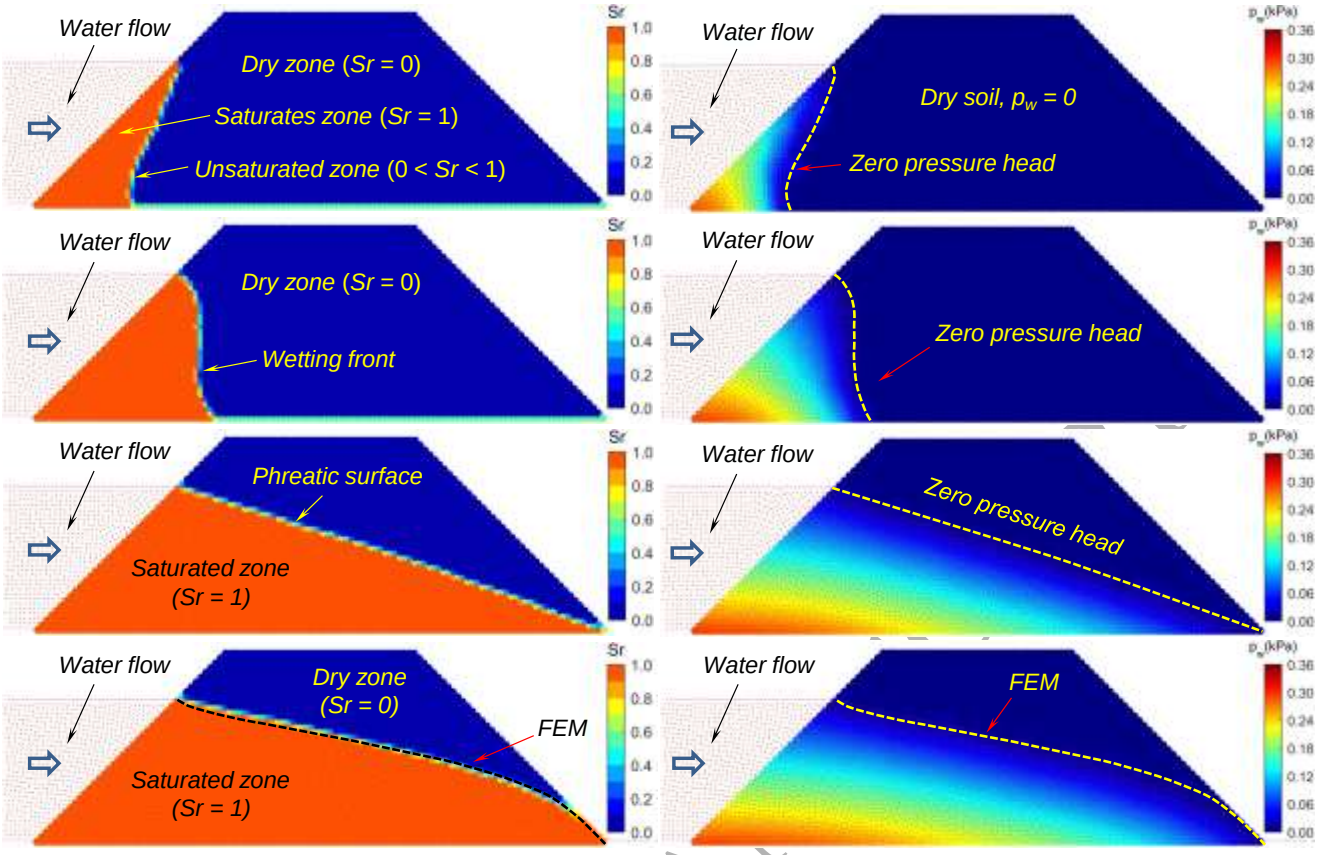

Figure 7: Evolutions of the saturated zone and the pore -water pressure distribution predicted by the two-phase SPH framework.

It can be seen that the progressive development of the seepage flow from the upstream slope to the downstream slope can be well described using the two-phase SPH framework. In the early stage of the development, the wetting front of the seepage flow develops rapidly in both vertical and horizontal directions owing to the rapid increase of water level in the reservoir. Subsequently, the wetting front mainly progresses in the horizontal direction in which the infiltration process occurs faster at the bottom slope due to the increase of pressure towards the bottom. After reaching the downstream slope toe, the wetting front gradually propagates upward due to the horizontal seepage force and finally reaches the steady stage at 1,151 seconds. The progressive development of the pore-water pressure inside the embankment shows a trend similar to that of the wetting front. A very smooth pore-water profile is obtained from the proposed two-phase SPH framework thanks to the explicit ISPH scheme employed. We noted that the weakly compressible SPH technique adopted in most previous two-phase SPH works showed pressure fluctuation. This can be compromised by adopting some recent SPH improvements such as using density filter techniques (Colagrossi and Landrini, 2003) or adding a diffuse term into the continuity equation (Antuono et al., 2010). However, the capability of these techniques to align the SPH simulation time to a long physical time problem is still questionable. The proposed explicit ISPH, on the other hand, can handle these problems without any problem owing to the fact that the density is reset after each time step to achieve the incompressibility assumption.

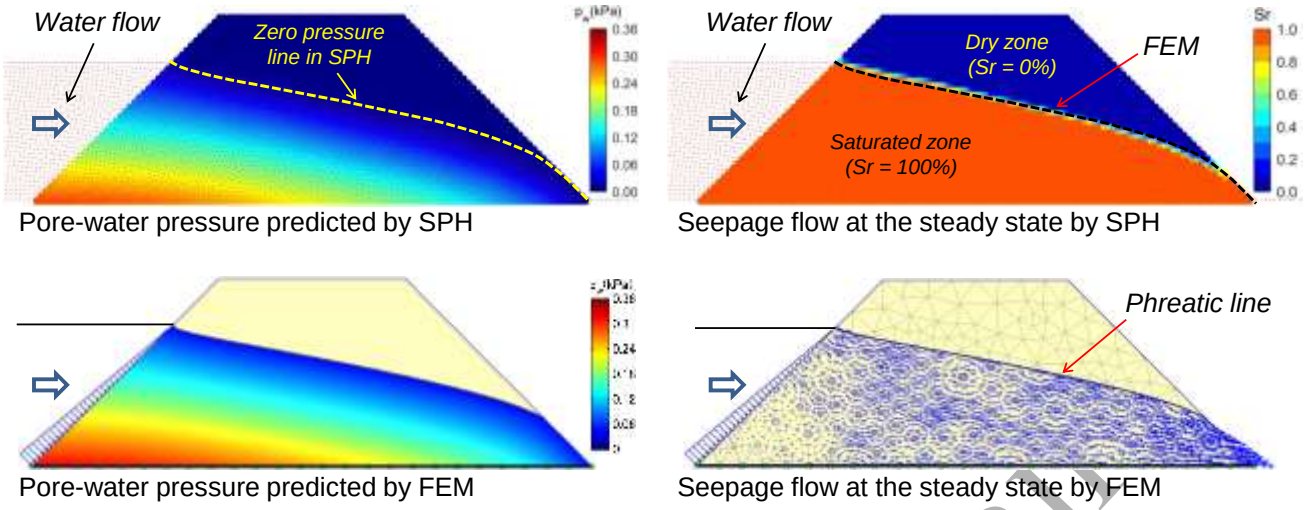

Figure 8: The final phreatic surface and the pore-water pressure distribution predicted by the two-phase SPH framework (upper) and the PLAXIS-FE model (lower).

The accuracy of the proposed two-phase SPH framework is further examined by comparing its solutions with those obtained by the PLAXIS FE-model. Because the PLAXIS FE-model could not simulate the transient coupled behaviour of seepage flow development shown in Figure 7, the final steady-state solutions are used as the benchmark for the SPH simulations. Figure 8 shows the comparison of the phreatic surface and the contour plot of the pore-water pressure distribution inside the embankment. There is a good agreement on the predictions of the ground water table by the SPH framework and PLAXIS FE-model. The final shape of the ground water table in both simulations is found to be a curve line with the upstream end normal to the upstream equipotential line (i.e. the upstream slope) and the downstream end tangent to the downstream slope. These results agree well with theoretical/graphical solutions as well as actual seepage behaviour through the earth dam reported in the literature. The pore-water pressure distributions of SPH and FEM solutions are in very good agreement and the pressure value at the upstream slope toe corresponds with the water level in the reservoir of 0.3 m. This suggests that the proposed two-phase SPH framework could achieve high accuracy in simulations of the seepage flow through earth structures.

5.3. Validation with experiments from CEDEX

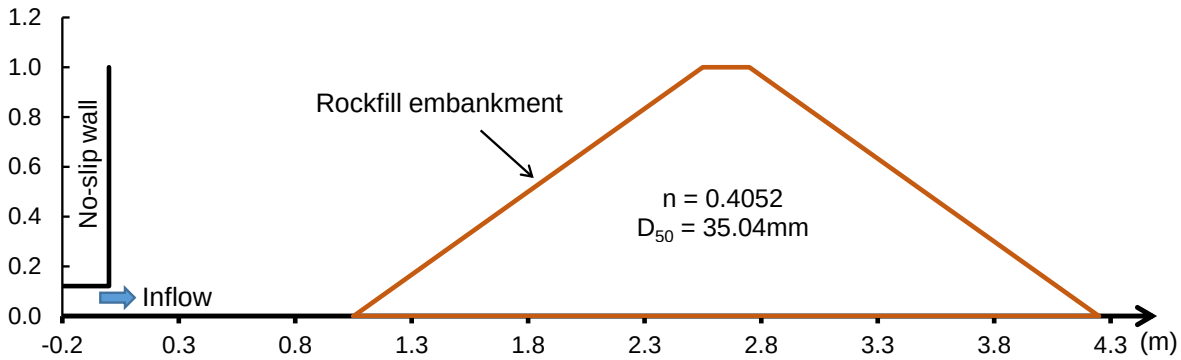

Figure 9: Geometry and setting conditions of the flow through a rockfill dam experiment.

In this validation test, the experiments on the steady state seepage flow through a rockfill dam from XPRESS and E-DAMS projects (Larese, 2012) are simulated using the proposed two-phase SPH

framework. These experiments were conducted in the Centre for Hydrographical Studies of CEDEX to investigate the seepage flow through rockfill dams and serve as benchmarks to validate a particle finite element method (PFEM) code. The geometry setting and boundary conditions of the rockfill dam (Case A1) is shown in Figure 9. The rockfill dam is 1 m high, 3.2 m wide; both the upstream and downstream slopes are 1.5:1.0. The dam was constructed in a flume of 2.64 m width with several built-in sensors at the bottom to record the pressure head and a regulation valve to control the incoming discharge. The rockfill material is quarry stone with D_{50} = 35.04 mm and the porosity of n_w = 0.4052. The dry and saturated densities are 1490 and 1910 kg/m^3 respectively. The incoming flow discharge of Q = 25.46 L/s is imposed on the upstream slope and the steady flow is achieved by keeping the constant flow rate. In order to provide experimentally validated data for the numerical simulations, several pressure sensors were installed on the bottom floor of the embankment at the distance of 2.75, 3.25, 3.75, 4.3m from the inlet water flow. These experimental data provide information on the phreatic surface inside the rockfill embankment at corresponding locations.

Owing to the nature of a rapid flow through high permeable rockfill porous media, the linear Darcy's law adopted to calculate the seepage force in the proposed two-phase SPH framework is no longer applicable. In fact, the linear Darcy's law is only valid for laminar flows in low permeability media where viscous forces are dominant, i.e. Reynolds numbers $Re \in [1-10]$ (Bear and Cheng, 2010). For a high flow rate through a highly permeable porous medium, i.e. $Re > 100$, the viscous force is dominated by the inertial force which tends to produce instabilities causing turbulence of the flow; thus, the flow rate is no longer linearly proportional to the pressure gradient (Bear and Cheng, 2010). Seepage flow through rockfill dams is an example of the flow through high permeable porous media, for which the linear Darcy's law is not applicable. In such cases, the nonlinear quadratic Darcy-Forchheimer's law with empirical coefficients taking into account the physical properties of the rockfill material such as the size, porosity and shape is widely employed (Larese, 2012). Accordingly, in this particular application, instead of using the seepage force based on the linear Darcy's law, i.e. Equation (18), the following quadratic Darcy-Forchheimer's resistance law with the Ergun's coefficients is adopted:

$$\mathbf{R} = -\left(n_w \frac{\mu}{k} \mathbf{v}_{ws} + \frac{1.75}{\sqrt{150}} \frac{\rho_w n_w}{\sqrt{k} n^{3/2}} \|\mathbf{v}_{ws}\| \mathbf{v}_{ws} \right) + p_w \nabla n_w \tag{91}$$

where $\mathbf{v}_{ws}$ is the relative vector velocity between water and soil particles; $\|\mathbf{v}_{ws}\|$ is the norm of the relative velocity; and k is the permeability coefficient defined as follows:

$$k = \frac{n_w^3 D_{50}^2}{150(1-n_w)^2} \tag{92}$$

with D_{50}^2 being the average diameter of the granular materials.

In the SPH simulation, the above rockfill dam is modelled by 4250 particles arranged in a regular square lattice with an initial spacing of 2 cm and a smoothing length of 2.4 cm. The rockfill dam is modelled as an elastic homogeneous material with the following material properties: Young's modulus E = 3.5 MPa and Poisson's ratio υ = 0.3. The incoming water flow is modelled by means of periodic boundary condition described in Section 4.2.2. For the incoming water flow of Q = 25.46 l/s, the inlet water velocity is u_{in} = 0.086 m/s, which corresponds to the height of the incoming flow zone of h_{in} = 0.12 cm, is adopted. No-slip boundary condition is applied to all boundaries for both water and solid phases. In order to save the computational time, any water particle that moves out of the rockfill dam and reaching the distance of 4.5 m is deleted from the computation. Similar to the previous test, the initial in-situ stress condition of the rockfill dam is obtained by applying the gravity loading to solid particles (Bui and Fukagawa, 2013). The convergence of the SPH numerical results are also investigated and it is confirmed that the numerical solution is converged at the spatial resolution of less than or equal to 2 cm.

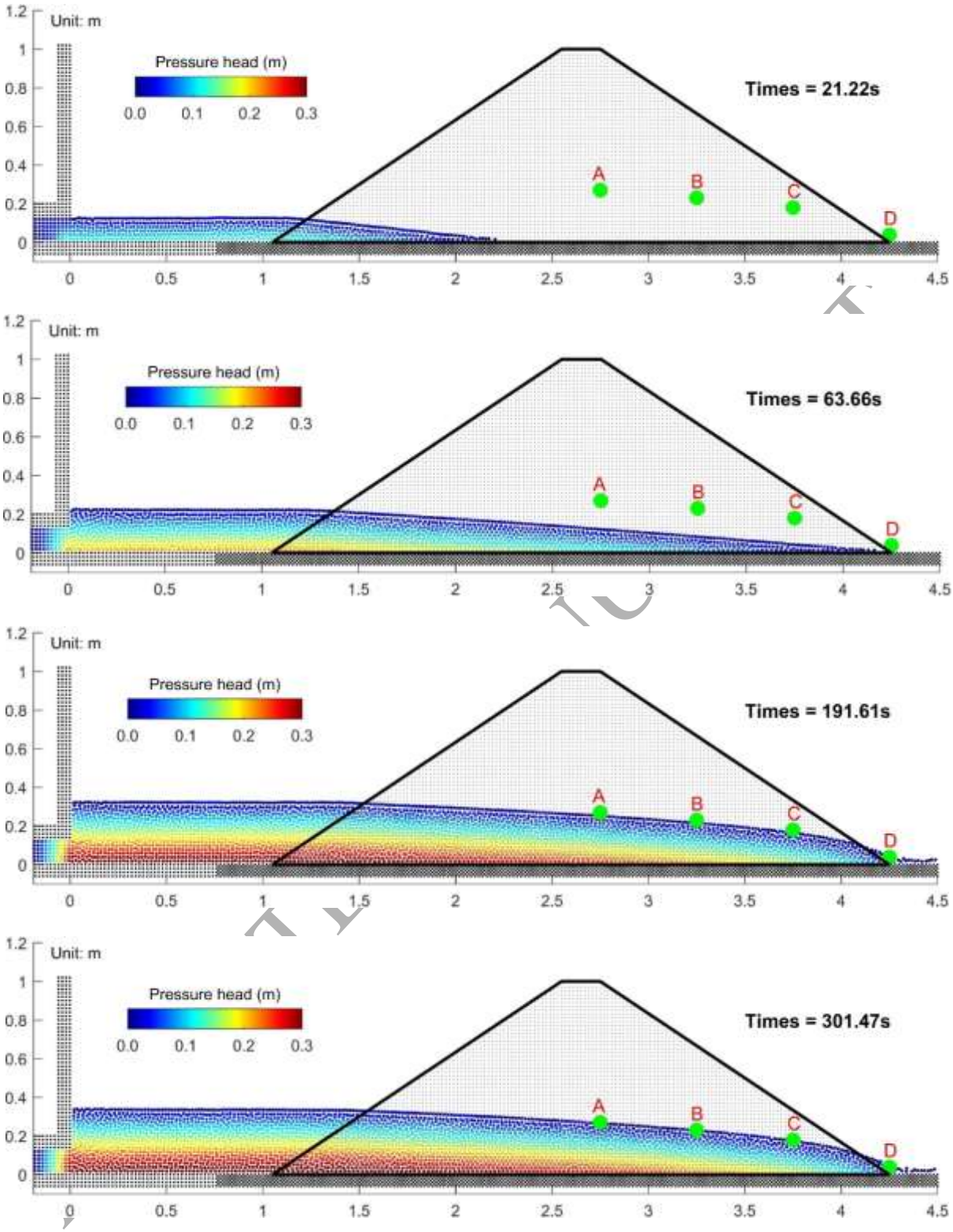

Figure 10: Progressive development of the phreatic surface predicted by the two-phase SPH framework.

Figure 10 shows the evolution of the water free-surface in the upstream reservoir and inside the rockfill dam at several time intervals. The green dots (A-D) represents the final steady-state of the phreatic surface obtained from the four pressure gauges installed at the distances of 1.70, 2.20, 2.70 and 3.25 m from the upstream slope toe in the experiment. It can be seen that the water level in the

reservoir increases as the water starts flowing in from the water inlet gate. Because of the high permeability of the rockfill material, the seepage flow inside the dam is mainly driven by the incoming flow velocity and progresses faster in the horizontal direction. It takes approximately 64 s for the water flow to reach the downstream slope toe. The phreatic surface inside the dam then rises simultaneously with the increase of the upstream water level in the reservoir. The steady state of the seepage flow in the simulation is achieved at around 300 s, although the water table has almost reached this level at around 190 s. Similarly to the previous test, the curved shape of the final water table inside the rockfill dam is also achieved. The predicted phreatic surface at the location of the pressure gauges agrees very well with those measured in the experiment (green dots A-D). In addition, the evolution of pressure heads at four locations with time is plotted in Fig. 14. As can be seen, steady state is reached at about 300 s, at which the pressure heads at four locations are stable and agree well with the experimental measurements. In short, thanks to the explicit ISPH model, the pressure profile of the water flow and the time evolution of the pressure profile at the four pressure gauges are very well simulated in the numerical model. Very smooth pressure profile is achieved in the SPH simulation for the water flow, both in the reservoir and inside the dam. Furthermore, the smooth transition of the pressure curve is obtained at all measurement points, except the one at the slope toe (Point D) which exhibits high pressure fluctuation. This result is expected due to the sudden change of water velocity from the inside porous medium to free-surface conditions. On the other hand, very high fluctuations of the pressure profile and pressure gauge curves will be obtained if the weakly compressible SPH model is adopted to simulate the water flow, as in previous works utilising this model (Bui et al., 2007; Grabe and Stefanova, 2015; Maeda and Sakai, 2010; Zhang and Maeda, 2015).

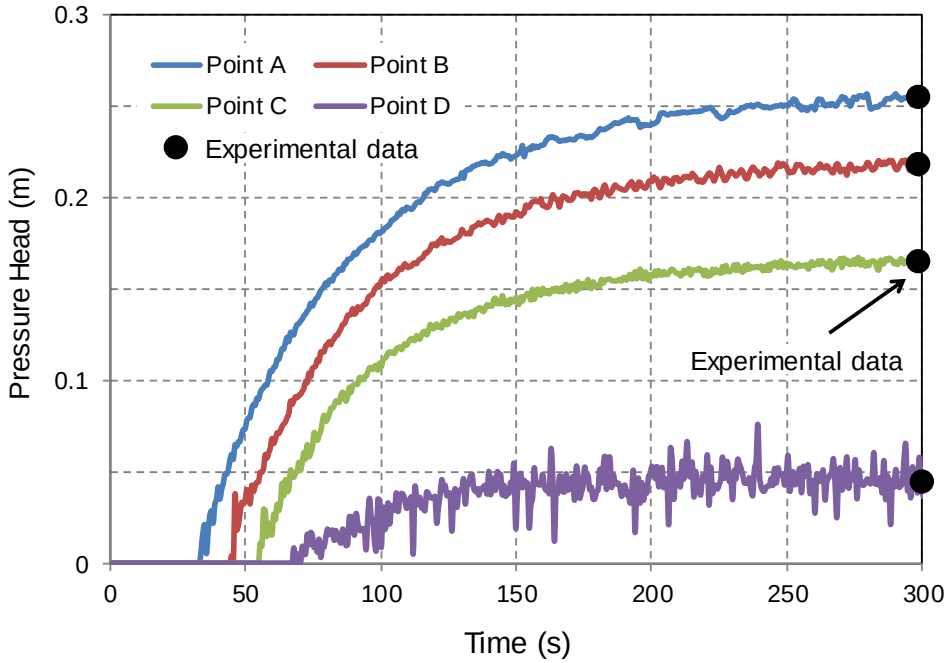

Figure 11: Evolution of pressure heads at four locations.

Comparing to the previous work utilising the PFEM to simulate the same seepage flow through the rigid rockfill dam (Larese, 2012), the SPH simulation takes a longer time to reach the steady-state water table level. This difference can be attributed to the no-slip boundary condition adopted in the current work for the fluid flow simulation. Nevertheless, both approaches only achieved good agreement with the experiment after adopting the seepage force model based on the quadratic Darcy-

Forchheimer's resistance law. Use of the seepage force model based on the linear Darcy's law in both the two-phase SPH model and PFEM led to significant underestimation of the experimentally observed final phreatic surface.

The influence of the material porosity on the steady-state phreatic surface is investigated by varying the porosity from n = 0.30, 0.35, 0.40 to 0.45, while keeping all other material properties and simulation conditions fixed. It can be seen from Figure 12 that a uniform increase of the porosity results in a uniform increase of the phreatic surface which is consistent with the finding of (Larese, 2012). Apparently, when the porosity reduces by 50% (from 0.45 to 0.30), the intrinsic permeability, calculated by Equation (92), declines more than 5 times, leading to an increase in the same amount of the first two terms of the resistance in Equation (91) which makes the phreatic surface increase significantly. The time to reach the final steady-state of the phreatic surface also increases as the porosity reduces.

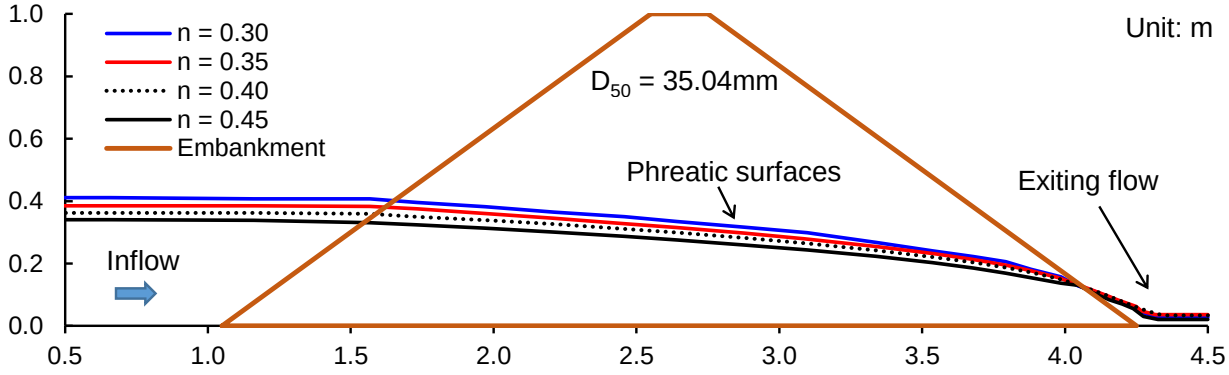

Figure 12: Influence of porosity n on the steady-state phreatic surface.

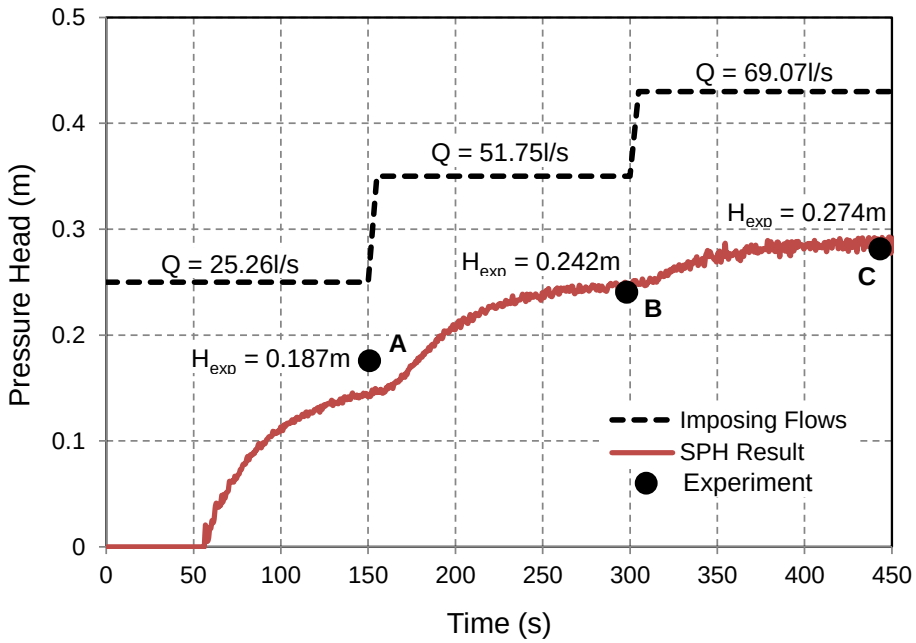

Figure 13: Evolution of the pressure head corresponding to raising inlet discharges.

Finally, the predictive capability of the proposed two-phase SPH framework is further examined to analyse the experiment of transitory incoming flow discharges, Case A2 reported in (Larese, 2012). This example serves as a demonstration of the capability of the proposed numerical framework to

model a practical flooding situation where flood curves of different incoming discharges can be used as an input. Three levels of incoming discharges of Q = 25.26, 51.75 and 69.07 l/s are imposed at the inflow gate in a total time of 450 s with a transition time of 10 s each to ensure smooth transitory regimes as well as sufficient time to reach a steady-state of each discharge in the experiment. The same geometry and boundary conditions employed in the previous rockfill dam SPH simulations are adopted in this test with the only difference being the incoming flow discharges. Figure 13 shows the imposed incoming discharges and the corresponding time evolution of the pressure head evaluated at the bottom floor at the location of 2.7 m from the upstream slope toe (i.e. back circle dots). The numerical results show that, for the first incoming flow discharge (Q = 25.26 l/s), the predicted flow does not fully reach the steady-state condition and therefore underestimates the measured pressure head (Point A). However, in the latter two incoming flow discharges (Q = 51.75 and 69.07 l/s), the flow predicted by the two-phase SPH reaches the steady-state and the predicted pressure heads agree well with the experimental measurements at the same locations (Points B & C). The underestimation of the SPH model for the first inlet discharge may be due to the Ergun's coefficients used in Equations (91) and (92). These coefficients were calibrated by (Larese, 2012) for PFEM simulations of the water flow through a rigid rockfill dam in which only the fluid model was employed. Because of those assumptions, full coupling between the fluid flow and the dam structure such as variation of permeability according to the change of void ratio or dam's deformation was not taken into account in their simulations. As a result, the calibrated Ergun's coefficients are only appropriate under the assumption of rigid dam. In fact, this assumption may not be appropriate in the early stage, in which rearrangement of the rockfill material might occur, before the water flow reaches the steady state corresponding to the first imposing discharge. It is more valid in the later stage of the experiment when there is no more deformation of the rockfill dam.

5.4. Application for a seepage flow-induced progressive failure

This section presents an application of the two-phase SPH framework to simulate a physical model test of seepage flow-induced large deformation and progressive failure of an embankment. The outline of the physical model test is firstly presented to set out the scene for the application. Subsequently, details of the SPH model and numerical results of the physical model test are presented and discussed.

5.4.1. Outline of the physical model test

The geometry and boundary conditions of the physical model test is similar to those shown in Figure 6. The embankment was made of Masa soil, which is a weathered granite typically found in Kansai area in Japan. The initial water content of slope was kept at approximately 5% and the corresponding soil properties are given in Table 1. The embankment is 400 mm in height and 400 mm in top-width with both upstream and downstream slopes of 1:1. The embankment was constructed in a flume made of stainless steel with the front-side covered by thick glass to monitor the failure surface. To reduce the sidewall boundary effect, lubricating oil was applied between the soil and the sidewall to minimise the friction. The test was started by gradually raising water in the upstream reservoir on the left-side of the embankment up to 30 cm in height and then kept constant at this level. Two cameras were setup on the front and side-views of the embankment to record the progressive failure of the downstream slope. The complete front view of the embankment is shown in Figure 14.

Figure 15 shows two typical snapshots of the embankment failure process. The first snapshot (Figure 15a) was taken when the downstream slope toe was deteriorated by the seepage flow causing a local failure zone in the downstream slope toe. At this stage, several failure surfaces were visible from the sidewall indicating the progressive failure. The failure mechanism of the slope toe can be attributed to the fact that the shear strength of the soil in this zone was significantly reduced owing to the reduction of soil matrix suction upon the soil wetting process. Losing the matrix suction, the soil becomes cohesionless and could be easily washed away by the seepage flow. The seepage front

continuously developed inside the embankment owing to the constant water supply from the upstream reservoir, leading to the enlargement of the local failure zone in the downstream slope toe. The continuous development of the local failure zone at the downstream slope toe due to the development of seepage force caused the downstream slope unstable, and eventually led to the catastrophic failure of the whole embankment (Figure 15b). The rotational failure mechanism was observed in the experiment with the loosen soil mass sliding along the major failure surface. The circular failure surface was reconstructed by removing the failure soil mass. A quite uniform rotational failure mechanism was achieved in the lateral direction, suggesting that the embankment failure experiment can be modelled under the 2D plane-strain condition.

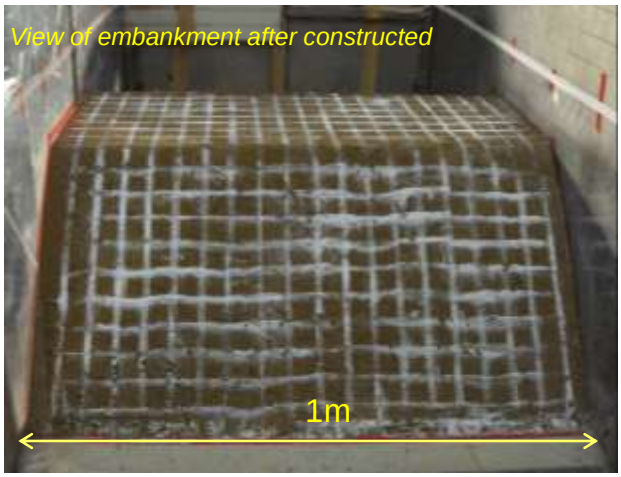

Table 1: Soil parameters used in simulations

Initial water content (w)	5(%)
Young's moduυlus (E)	3 Mpa
Poisson ratio (υ)	0.3
Friction angle (ϕ)	31.2 deg
Initial cohesion (c)	0.55 kPa
Dilatancy angle (ψ)	10 deg
Particle density (ρ_s)	2.6 (g/cm^3)
Initial porosity (n)	0.4
Initial permeability (k_o)	1.1×10^{-4}m/s

Figure 14: The completed view of the embankment after constructed.

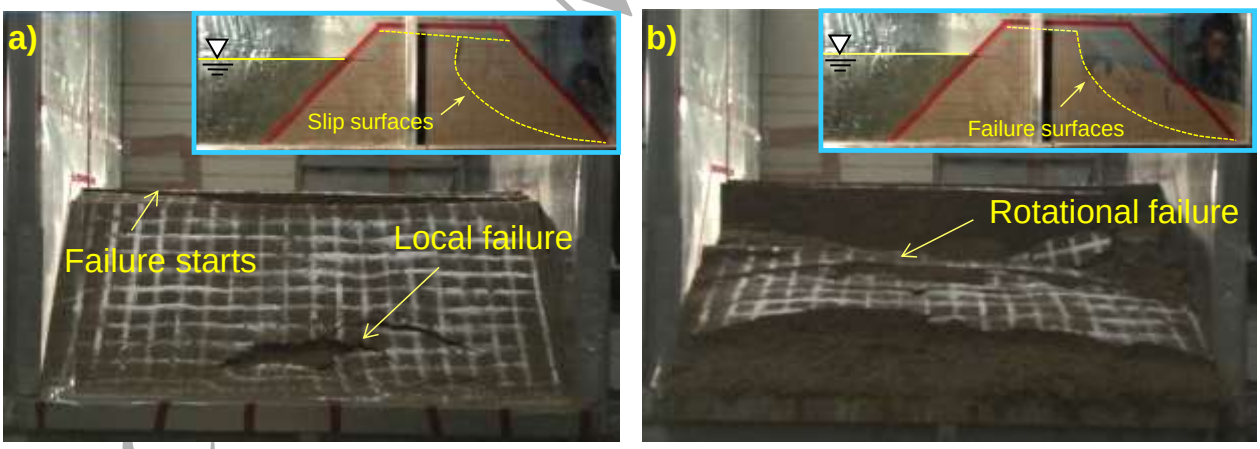

Figure 15: Failure progress of the embankment in the experiment.

5.4.2. Numerical prediction of the embankment collapse using the two-phase SPH model

As discussed above, owing to the relatively uniform lateral deformation observed in the experiment (see Figure 15), the embankment failure experiment can be considered in the plane-strain configuration with homogenous soil properties. Thus, the 2D two-phase SPH framework can be used for the simulation of the above seepage flow induced embankment failure. An elasto-plastic model employing the Drucker-Prager yield criterion described in Section 2.5 is adopted to describe the behaviour of the soil, with the material properties given in Table 1. The simple strength reduction model, i.e. Equation (36), is adopted to account for the influence of saturation degree on the soil cohesion, and thus the reduction of soil matrix suction due to the wetting process observed in the

experiment. In particular, the soil cohesion reduces linearly from c_o = 0.55 kPa to c_{sat} = 0.01 kPa which corresponds to the increase of saturation degree from S_r = 0.05 to S_r = 1, respectively. The inclusion of the small cohesion of c_{sat} = 0.01kPa to the fully saturated soil is to account for the interlocking behaviour of soil owing to different particle shapes in reality. As for the seepage force model, due to the relatively small permeability of the current sandy soil, the seepage force model based on the linear Darcy's law is adopted in the simulation. All other geometry setting and boundary conditions follow the previous numerical model described in Section 5.2. In addition, prior to running the seepage flow induced embankment failure simulation, the initial in-situ stress condition of the embankment is obtained by applying the gravity loading to soil particles (Bui and Fukagawa, 2013).

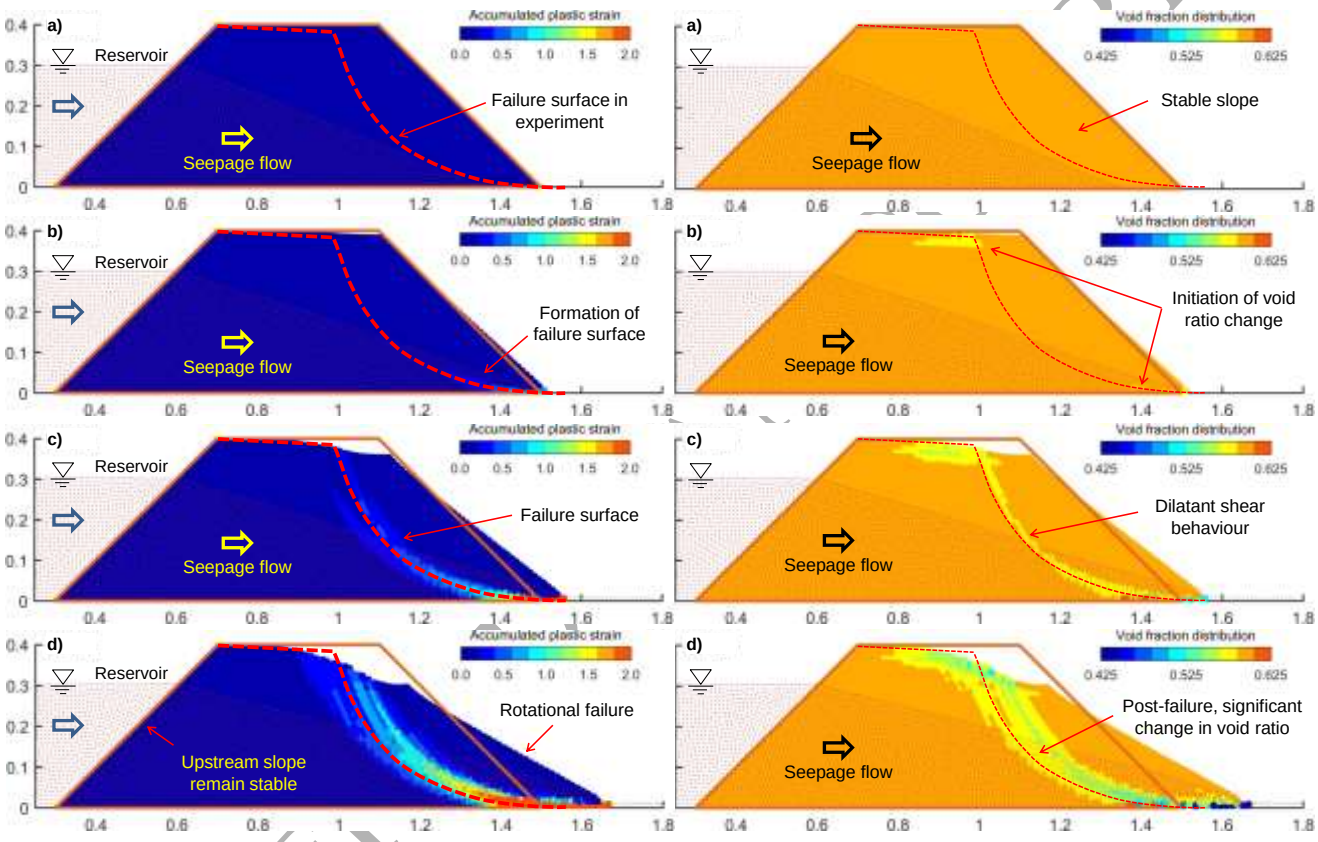

Figure 16: Progressive failure of the embankment predicted by SPH.

Figure 16 shows the progressive failure process of the embankment induced by the seepage flow with the embedded failure surface observed in the experiment (i.e. dashed line). On the left side of Figure 16 are plots of the accumulated plastic strain whereas plots of the void fraction distribution in the embankment during the post-failure process of the embankment are presented on the right side of the figure. Before the seepage flow gets to the downstream slope toe, the deformation of the embankment is negligible although the saturated zone has a very low cohesion of c_{sat} = 0.01kPa (Figure 16a). As soon as the seepage flow reaches the downstream slope toe, the soil in this region loses its shear strength, triggering the failure of the embankment. The failure process starts by a dramatic change of the plastic strain and the void ratio at the downstream slope toe as well as a minor settlement of the downstream crest of the embankment (Figure 16b). Comparing with the experiment, although the two-phase SPH model could not reproduce the local failure zone observed at the downstream slope toe in the experiment (Figure 15a), the model is able to capture the major

mechanism triggering the embankment failure which is initiated from the downstream slope toe. Subsequently, starting from the downstream slope toe, the first shear band presented by the concentration of high plastic strains progressively develops upward following the experimentally-observed major failure surface to the crest of the embankment. This localisation failure band corresponds to the loosening soil area developed due to the dilation behaviour of the soil subjected to shearing. In particular, soil particles along the shear band separate from each other because of a large amount of plastic volume change developed during the post-failure regime, causing the void fraction of the soil along the shear band to reduce. Corresponding to the generation of this localisation band, the downstream soil mass starts tilting along this main potential slip surface (Figure 16c). As the water flow continues, the downstream slope completely fails in the tilting mode illustrated by a large shear zone which divides the soil mass into two zones on the left and the right with negligible deformation or void fraction change (Figure 16d). On the other hand, the upstream slope remains stable although the cohesion of the saturated zone significantly reduces. This is thanks to the retaining water pressure from the upstream reservoir which is automatically achieved through Equation (63). At the final stage (Figure 16d), a significant reduction of the solid void fraction is observed at the downstream toe where the seepage flow goes out of the embankment, which clearly indicates the influence of the seepage force. The final shear zone also consists of one main slip surface developed from the initial-potential slip surface in Figure 15c and several secondary ones which are also observed in the experiment. On the other hand, the discontinuous and cracking deformations on the downstream slope surface observed in the experiment (Figure 15b) could not be reproduced in the current SPH simulation due to the simplification of the soil constitutive model. In order to capture this behaviour, advanced unsaturated soil models (Alonso et al., 1990; Khalili and Loret, 2001; Loret and Khalili, 2000; Sheng et al., 2008) should be adopted and these are beyond the scope of this paper.

The above numerical applications demonstrate the capability of the proposed SPH approach in handling coupled problems involving complex water free-surface/seepage flows and large deformation of soils, which are difficult to be modelled using FEM-based approaches. However, owing to the requirement of two different Lagrangian discretisations to represent the solid and fluid phases, the proposed SPH approach generally incurs more computational cost than FEM-based approaches, in which a single discretisation mesh consisting finite elements with different shape functions are used to solve the governing equations of the mixture. Nevertheless, the numerical implementation of the proposed SPH approach is straightforward as computation domains are merely discretised using points (particles), which are arranged in a regular square lattice. Special attentions might be required to handle complex boundary conditions such as curvature solid boundaries. These are however beyond the scope of this paper.

6. CONCLUSIONS

This paper presents the development of a new two-phase SPH framework to enhance the predictive capability of existing computational approaches to study the coupled fluid-solid interaction in deformable porous media. The framework is a significant advancement from the original coupled two-phase SPH approach proposed by the first author (Bui et al., 2007) that includes the following key features: 1) two layers of Lagrangian particles are used to represent solid and fluid phases which are solved simultaneously using their own governing equations; 2) effects of void fractions on the coupling behaviour of two phases are fully considered; 3) pore-pressure coupled with matrix soil deformation is considered for the first time within the SPH context; 4) a fully consistent mathematical framework to achieve stable SPH numerical solutions is described; and 5) a stable SPH solution for an incompressible fluid flow that is aligned to long physical time problems. The proposed two-phase SPH framework, in our opinion, is unique in the sense that it can be applied to a

wide range of problems, including those which are unable to be resolved using traditional FEM-based coupled approach, such as scour due to overtopping flow, internal erosion due to seepage flow, transportation of contaminated substances in subsurface, submarine landslides, etc. The proposed two-phase SPH framework was first validated against analytical solutions for initial in-situ stresses of fully submerged soil under gravity loading. Next, the framework was validated with the PLAXIS FE-model and experiments for the seepage flow through low and high permeable porous media, respectively. Finally, the framework was employed for the simulation of a physical model test of seepage flow induced embankment failure that involves large deformations. Very good agreements with analytical solutions, PLAXIS FE-model and experiments were achieved, suggesting that the proposed two-phase SPH-framework is a promising approach for the study of coupled fluid-solid interaction in deformable porous media that involve large deformations and failures of the solid phase. In order to further advance the proposed two-phase SPH framework, unsaturated soil constitutive models should be adopted to replace the simple elasto-plastic constitutive model utilised in the current work. Furthermore, the modelling of post-failure behaviour of soils needs further improvements as this process often involves fluidised flow behaviour and fractures on the soil surfaces that are unable to model using existing constitutive models. On the other hand, computational algorithm is also another topic that is worth to pay attention to, in order to reduce computational costs required to simultaneously solve two layers of Lagrangian particles in the two-phase SPH platform.

ACKNOWLEDGEMENT

Funding support from the Australian Research Council via projects DP160100775 (Ha H. Bui), FT140100408 (Giang D. Nguyen) and DP170103793 (Nguyen & Bui) is gratefully acknowledged. The authors would like to thank Mr. Chi T. Nguyen for his help in collecting rockfill experimental data for the validation of the proposed numerical framework.

REFERENCES

Alonso, E. E., A. Gens, and A. Josa, 1990, A Constitutive Model for Partially Saturated Soils: Geotechnique, v. 40, p. 405-430.

Antuono, M., A. Colagrossi, S. Marrone, and D. Molteni, 2010, Free-surface flows solved by means of SPH schemes with numerical diffusive terms: Computer Physics Communications, v. 181, p. 532-549.

Bear, J., and A. H. D. Cheng, 2010, Modeling groundwater flow and contaminant transport: Theory and applications of transport in porous media: Dordrecht ; London, Springer, xxi, 834 p. p.

Belytschko, T., Y. Y. Lu, and L. Gu, 1994, Element-Free Galerkin Methods: International Journal for Numerical Methods in Engineering, v. 37, p. 229-256.

Biot, M. A., 1956, Theory of Propagation of Elastic Waves in a Fluid-Saturated Porous Solid: Journal of the Acoustical Society of America, v. 28, p. 168-191.

Blanc, T., and M. Pastor, 2012, A stabilized Fractional Step, Runge-Kutta Taylor SPH algorithm for coupled problems in geomechanics: Computer Methods in Applied Mechanics and Engineering, v. 221, p. 41-53.

Blanc, T., and M. Pastor, 2013, A stabilized Smoothed Particle Hydrodynamics, Taylor-Galerkin algorithm for soil dynamics problems: International Journal for Numerical and Analytical Methods in Geomechanics, v. 37, p. 1-30.

Bowen, R. M., 1976, Theory of Mixtures, *in* A. C. Eringen, ed., Continuum Physics, v. III: New York, Academic Press, p. 1-127.

Bui, H. H., and R. Fukagawa, 2009, A first attempt to solve soil-water coupled problem by SPH: Japanese Terramechanics, v. 29, p. 33-38.

Bui, H. H., and R. Fukagawa, 2013, An improved SPH method for saturated soils and its application to investigate the mechanisms of embankment failure: Case of hydrostatic pore-water pressure: International Journal for Numerical and Analytical Methods in Geomechanics, v. 37, p. 31-50.

Bui, H. H., R. Fukagawa, and K. Sako, 2006, Smoothed particle hydrodynamics for soil mechanics: Proceedings of the 6th European Conference on Numerical Methods in Geotechnical Engineering - Numerical Methods in Geotechnical Engineering, p. 278-281.

Bui, H. H., R. Fukagawa, K. Sako, and S. Ohno, 2008, Lagrangian meshfree particles method (SPH) for large deformation and failure flows of geomaterial using elastic-plastic soil constitutive model: International Journal for Numerical and Analytical Methods in Geomechanics, v. 32, p. 1537-1570.

Bui, H. H., R. Fukagawa, K. Sako, and J. C. Wells, 2011a, Slope stability analysis and discontinuous slope failure simulation by elasto-plastic smoothed particle hydrodynamics (SPH): Geotechnique, v. 61, p. 565-574.

Bui, H. H., J. K. Kodikara, A. Bouazza, A. Haque, and P. G. Ranjith, 2014, A novel computational approach for large deformation and post-failure analyses of segmental retaining wall systems: International Journal for Numerical and Analytical Methods in Geomechanics, v. 38, p. 1321-1340.

Bui, H. H., K. Sako, and R. Fukagawa, 2007, Numerical simulation of soil-water interaction using smoothed particle hydrodynamics (SPH) method: Journal of Terramechanics, v. 44, p. 339-346.

Bui, H. H., K. Sako, R. Fukagawa, and C. T. Nguyen, 2011b, An investigation of riverbank failure due to water level change using two-phase fl ow SPH model: Computer Methods for Geomechanics: Frontiers and New Applications, p. 116-123.

Cascini, L., S. Cuomo, M. Pastor, and G. Sorbin, 2010, Modeling of Rainfall-Induced Shallow Landslides of the Flow-Type: Journal of Geotechnical and Geoenvironmental Engineering, v. 136, p. 85-98.

Chen, W., and T. Qiu, 2012, Numerical Simulations for Large Deformation of Granular Materials Using Smoothed Particle Hydrodynamics Method: International Journal of Geomechanics, v. 12, p. 127-135.

Colagrossi, A., and M. Landrini, 2003, Numerical simulation of interfacial flows by smoothed particle hydrodynamics: Journal of Computational Physics, v. 191, p. 448-475.

Deb, D., and R. Pramanik, 2013, Failure Process of Brittle Rock Using Smoothed Particle Hydrodynamics: Journal of Engineering Mechanics, v. 139, p. 1551-1565.

Duan, Q. L., and T. Belytschko, 2009, Gradient and dilatational stabilizations for stress-point integration in the element-free Galerkin method: International Journal for Numerical Methods in Engineering, v. 77, p. 776-798.

Ehlers, W., T. Graf, and M. Ammann, 2004, Deformation and localization analysis of partially saturated soil: Computer Methods in Applied Mechanics and Engineering, v. 193, p. 2885-2910.

Fredlund, D. G., and H. Rahardjo, 1993, Soil mechanics for unsaturated soils: New York, Wiley, xxiv, 517 p. p.

Gambolati, G., M. Ferronato, P. Teatini, R. Deidda, and G. Lecca, 2001, Finite element analysis of land subsidence above depleted reservoirs with pore pressure gradient and total stress formulations: International Journal for Numerical and Analytical Methods in Geomechanics, v. 25, p. 307-327.

Gelet, R., B. Loret, and N. Khalili, 2012, A thermo-hydro-mechanical coupled model in local thermal non-equilibrium for fractured HDR reservoir with double porosity: Journal of Geophysical Research-Solid Earth, v. 117.

Gingold, R. A., and J. J. Monaghan, 1977, Smoothed Particle Hydrodynamics - Theory and Application to Non-Spherical Stars: Monthly Notices of the Royal Astronomical Society, v. 181, p. 375-389.

Grabe, J., and B. Stefanova, 2015, Numerical modeling of saturated soils based on smoothed particle hydrodynamics (SPH): Geotechnik, v. 38, p. 218-229.

Gray, J. P., J. J. Monaghan, and R. P. Swift, 2001, SPH elastic dynamics: Computer Methods in Applied Mechanics and Engineering, v. 190, p. 6641-6662.

Huang, Y., W. J. Zhang, Z. L. Dai, and Q. Xu, 2013, Numerical simulation of flow processes in liquefied soils using a soil-water-coupled smoothed particle hydrodynamics method: Natural Hazards, v. 69, p. 809-827.

Khalili, N., and B. Loret, 2001, An elasto-plastic model for non-isothermal analysis of flow and deformation in unsaturated porous media: formulation: International Journal of Solids and Structures, v. 38, p. 8305-8330.

Krysl, P., and T. Belytschko, 1996, Analysis of thin shells by the element-free Galerkin method: International Journal of Solids and Structures, v. 33, p. 3057-3078.

Larese, A., 2012, A coupled Eulerian-PFEM model for the simulation of overtopping in rockfill dams: Ph.D. Thesis thesis, UPC BarcelonaTech, Barcelona, Spain, 258p p.

Lastiwka, M., M. Basa, and N. J. Quinlan, 2009, Permeable and non-reflecting boundary conditions in SPH: International Journal for Numerical Methods in Fluids, v. 61, p. 709-724.

Leroch, S., M. Varga, S. J. Eder, A. Vernes, M. R. Ripoll, and G. Ganzenmuller, 2016, Smooth particle hydrodynamics simulation of damage induced by a spherical indenter scratching a viscoplastic material: International Journal of Solids and Structures, v. 81, p. 188-202.

Lewis, R. W., and H. R. Ghafouri, 1997, A novel finite element double porosity model for multiphase flow through deformable fractured porous media: International Journal for Numerical and Analytical Methods in Geomechanics, v. 21, p. 789-816.

Lewis, R. W., and Y. Sukirman, 1994, Finite-Element Modeling for Simulating the Surface Subsidence above a Compacting Hydrocarbon Reservoir: International Journal for Numerical and Analytical Methods in Geomechanics, v. 18, p. 619-639.

Libersky, L. D., A. G. Petschek, T. C. Carney, J. R. Hipp, and F. A. Allahdadi, 1993, High-Strain Lagrangian Hydrodynamics - a 3-Dimensional Sph Code for Dynamic Material Response: Journal of Computational Physics, v. 109, p. 67-75.

Loret, B., and N. Khalili, 2000, A three-phase model for unsaturated soils: International Journal for Numerical and Analytical Methods in Geomechanics, v. 24, p. 893-927.

Lucy, L. B., 1977, Numerical Approach to Testing of Fission Hypothesis: Astronomical Journal, v. 82, p. 1013-1024.

Maeda, K., and H. Sakai, 2010, Seepage Failure and Erosion of Ground with Air Bubble Dynamics, In Geoenvironmental engineering and geotechnics: progress in modeling and applications, USA, American Society of Civil Engineers (ASCE), p. 261–266.

Monaghan, J. J., 1994, Simulating Free-Surface Flows with Sph: Journal of Computational Physics, v. 110, p. 399-406.

Monaghan, J. J., 1997, Implicit SPH drag and dusty gas dynamics: Journal of Computational Physics, v. 138, p. 801-820.

Monaghan, J. J., 2012, Smoothed Particle Hydrodynamics and Its Diverse Applications: Annual Review of Fluid Mechanics, Vol 44, v. 44, p. 323-346.

Monaghan, J. J., and J. C. Lattanzio, 1985, A Refined Particle Method for Astrophysical Problems: Astronomy & Astrophysics, v. 149, p. 135-143.

Nguyen, C. T., C. T. Nguyen, H. H. Bui, G. D. Nguyen, and R. Fukagawa, 2017, A new SPH-based approach to simulation of granular flows using viscous damping and stress regularisation: Landslides, v. 14, p.

69-81.
Nomeritae, E. Daly, S. Grimaldi, and H. H. Bui, 2016, Explicit incompressible SPH algorithm for free-surface flow modelling: A comparison with weakly compressible schemes: Advances in Water Resources, v. 97, p. 156-167.
Onate, E., S. R. Idelsohn, F. Del Pin, and R. Aubry, 2004, The Particle Finite Element Method - an Overview: International Journal of Computational Methods, v. 1, p. 267-307.
Pastor, M., B. Haddad, G. Sorbino, S. Cuomo, and V. Drempetic, 2009, A depth-integrated, coupled SPH model for flow-like landslides and related phenomena: International Journal for Numerical and Analytical Methods in Geomechanics, v. 33, p. 143-172.
Peric, D., G. F. Zhao, and N. Khalili, 2014, Strain Localization in Unsaturated Elastic-Plastic Materials Subjected to Plane Strain Compression: Journal of Engineering Mechanics, v. 140.
Popescu, R., J. H. Prevost, G. Deodatis, and P. Chakrabortty, 2006, Dynamics of nonlinear porous media with applications to soil liquefaction: Soil Dynamics and Earthquake Engineering, v. 26, p. 648-665.
Prevost, J. H., 1980, Mechanics of Continuous Porous-Media: International Journal of Engineering Science, v. 18, p. 787-800.
Prevost, J. H., 1982, Non-Linear Transient Phenomena in Saturated Porous-Media: Computer Methods in Applied Mechanics and Engineering, v. 30, p. 3-18.
Prevost, J. H., 1985, Wave propagation in fluid-saturated porous media: An efficient finite element procedure: International Journal of Soil Dynamics and Earthquake Engineering, v. 4, p. 183–202.
Shao, S. D., and E. Y. M. Lo, 2003, Incompressible SPH method for simulating Newtonian and non-Newtonian flows with a free surface: Advances in Water Resources, v. 26, p. 787-800.
Sheng, D., D. G. Fredlund, and A. Gens, 2008, A new modelling approach for unsaturated soils using independent stress variables: Canadian Geotechnical Journal, v. 45, p. 511-534.
Sulsky, D., 1996, Application of a particle-in-cell method to solid mechanics (vol 87, pg 236, 1995): Computer Physics Communications, v. 96, p. 105-106.
Vangenuchten, M. T., 1980, A Closed-Form Equation for Predicting the Hydraulic Conductivity of Unsaturated Soils: Soil Science Society of America Journal, v. 44, p. 892-898.
Zhang, D. Z., X. Ma, and P. T. Giguere, 2011, Material point method enhanced by modified gradient of shape function: Journal of Computational Physics, v. 230, p. 6379-6398.
Zhang, W., and K. Maeda, 2015, SPH simulations for slope and levee failure under heavy rainfall considering the effect of air phase: Computer Methods and Recent Advances in Geomechanics, p. 1465-1470.
Zhang, X., K. Krabbenhoft, D. M. Pedroso, A. V. Lyamin, D. Sheng, M. V. da Silva, and D. Wang, 2013, Particle finite element analysis of large deformation and granular flow problems: Computers and Geotechnics, v. 54, p. 133-142.
Zienkiewicz, O. C., A. H. C. Chan, M. Pastor, B. A. Schrefler, and T. Shiomi, 1999, Computational geomechanics with special reference to earthquake engineering: New York, John Wiley & Sons, xi, 383 p., 2 p. of plates p.
Zienkiewicz, O. C., M. S. Huang, and M. Pastor, 1995, Localization Problems in Plasticity Using Finite-Elements with Adaptive Remeshing: International Journal for Numerical and Analytical Methods in Geomechanics, v. 19, p. 127-148.
Zienkiewicz, O. C., and T. Shiomi, 1984, Dynamic behaviour of saturated porous media; The generalized Biot formulation and its numerical solution International Journal for Numerical and Analytical Methods in Geomechanics Volume 8, Issue 1: International Journal for Numerical and Analytical Methods in Geomechanics, v. 8, p. 71-96.